Geophysical Journal International

Geophys. J. Int. (2024) **239,** 725–753
Advance Access publication 2024 August 22
GJI Geomagnetism and Electromagnetism

https://doi.org/10.1093/gji/ggae294

Plesio-geostrophy for Earth's core – II: thermal equations and onset of convection

Stefano Maffei,[1] Andrew Jackson[1] and Philip W. Livermore[2]

[1]*Institute for Geophysics, ETH Zurich, Sonneggstrasse 5, 8092 Zurich, Switzerland. E-mail: maffei.ste@gmail.com*
[2]*School of Earth and Environment, University of Leeds, Leeds, LS2 9JT, UK*

Accepted 2024 August 15. Received 2024 August 15; in original form 2024 January 3

SUMMARY

The columnar-flow approximation allows the development of computationally efficient numerical models tailored to the study of the rapidly rotating dynamics of Earth's fluid outer core. In this paper, we extend a novel columnar-flow formulation, called Plesio-Geostrophy (PG) by including thermal effects and viscous boundary conditions. The effect of both no-slip and stress-free boundaries, the latter being a novelty for columnar-flow models, are included. We obtain a set of fully 2-D evolution equations for fluid flows and temperature where no assumption is made regarding the geometry of the latter, except in the derivation of an approximate thermal diffusion operator. To test the new PG implementation, we calculated the critical parameters for onset of thermal convection in a spherical domain. We found that the PG model prediction is in better agreement with unapproximated, 3-D calculations in rapidly rotating regimes, compared to another state-of-the-art columnar-flow model.

Key words: Core; Dynamo: theories and simulations; Numerical approximations and analysis; Numerical modelling.

1 INTRODUCTION

Convective motions in Earth's fluid outer core are of paramount importance for understanding the geodynamo mechanisms responsible for the existence of the geomagnetic field. Given the impossibility of direct observation, numerical geodynamo simulations (Christensen & Wicht 2015; Wicht & Sanchez 2019; Landeau *et al.* 2022), in which the temporal evolution of fluid flows, magnetic fields and temperature are solved from a given initial condition, are currently the main tool for studying the dynamics of Earth's outer core. However, these kind of simulations are computationally very expensive, and can only partly access the extreme planetary regimes characterized by very low viscosity, rapid rotation, highly turbulent flows and a vast range of spatio-temporal scales. The dynamical regime of the core is typically characterized by the Ekman number, E, the ratio of rotational over viscous timescales and the Reynolds number Re, the ratio of viscous over advective timescales. Estimates for Earth are $E = O(10^{-15})$, $Re = O(10^{9})$ (e.g. Schaeffer *et al.* 2017), indicating both highly turbulent regimes and the profound impact of rotation on the dynamics. Conversely 3-D direct numerical simulations (DNSs) and laboratory experiments of convectively driven dynamics are typically performed in regimes characterized by $E \gtrsim 10^{-8}$ and $Re \lesssim 10^{3}$ (Kunnen *et al.* 2010; Sheyko 2014; Sheyko *et al.* 2016, 2018; ; Schaeffer *et al.* 2017; Rajaei *et al.* 2018; Guervilly *et al.* 2019; Long *et al.* 2020; Cheng *et al.* 2020; Calkins *et al.* 2021), depending on setup and study scope.

The limitations of 3-D methodologies have fuelled the search for reduced models, capable of reaching parameter regimes that are precluded from current DNS approaches. One successful family of models is rooted in the recognition that rotation is expected to be dominant in the force balance of Earth's core and other planetary fluid interiors. Geodynamo simulations at progressively lower E (Christensen & Wicht 2015), and aimed at reproducing features derived from geomagnetic field observations, further enforce the expectation that, in Earth' s core, the dynamics is strongly influenced by planetary rotation. Rapidly rotating fluid dynamics is characterized by a large separation in both spatial and temporal scales. In particular the vertical scales, along the direction parallel to the rotation axis, tend to be much larger than along the perpendicular direction (Davidson 2013). In enclosed domains, such as a sphere, this results in the formation of Taylor columns, spanning the whole of the vertical extension of the domain. A strong tendency for the formation of such columns has been confirmed in geodynamo simulations (Christensen & Wicht 2015) and is in agreement with estimates of large-scale flows at the top of the core being primarily symmetric about the equatorial plane (Holme 2015).

This consideration is the foundation of the models in the class termed columnar-flow models, in which it is assumed that horizontal motions (i.e. perpendicular to the rotation axis) are invariant along the rotation axis. This leads to a 2-D description of the fluid motions in

the core, and to numerical models that are computationally cheaper than traditional 3-D ones. In the context of the study of Earth's core, this approximation is often called quasi-geostrophic, or QG (e.g. Charney 1948; Schaeffer & Cardin 2005a, b; Canet *et al.* 2009). However, we choose to refer to it here as 'columnar' (Cardin & Olson 1994), to avoid confusion with other flavours of quasi-geostrophic theories used in the context of planetary interiors (e.g. Julien *et al.* 2006).

The columnar-flow approximation has proven extremely successful in the study of rapidly rotating convective dynamics, where magnetic effects are neglected (Aubert *et al.* 2003; Calkins *et al.* 2012; Guervilly & Cardin 2016; Guervilly *et al.* 2019; Barrois *et al.* 2022). These studies have proven their ability to simulate highly forced dynamics with a lower computational cost compared to that of 3-D DNS, allowing access to more planetary-like parameter-regimes. In a full-sphere geometry, where the presence of the inner core is neglected, it has been shown that the results of columnar-flow models agree well with DNS, when the same rapidly rotating regimes are simulated (Guervilly & Cardin 2016; Guervilly *et al.* 2019). Some reservations remain in spherical shell geometries, where the existence of the inner core leads to mathematical and physical inconsistencies (Barrois *et al.* 2022).

In the context of the oscillatory dynamics of Earth's core, where the presence of magnetic field is important, the columnar-flow approximation has been shown to be valid on inter-annual to decadal timescales (Jault 2008; Gillet *et al.* 2011). On these timescales the columnar approximation has proven capable of reproducing wave-like dynamics observed in high-quality geomagnetic data from ground- and satellite-observations (Gerick *et al.* 2021; Gillet *et al.* 2022).

The most recent columnar-flow implementations are of hybrid nature, where the momentum equation describes the temporal evolution of a 2-D stream-function, but magnetic fields and temperature anomalies are treated in their unapproximated, 3-D form (Guervilly & Cardin 2016; Guervilly *et al.* 2019; Gerick *et al.* 2021; Gillet *et al.* 2022; Barrois *et al.* 2022). While this approach does not require additional assumptions or complex manipulations of the magnetic field and temperature equations, the mixed nature of the variables solved for, introduces the need to perform precise vertical integration (see appendix D of Barrois *et al.* (2022) for some details). Alternative implementations have assumed a purely 2-D or columnar-like form for temperature (Guervilly & Cardin 2016; Guervilly *et al.* 2019; Barrois *et al.* 2022) or magnetic fields, (Canet *et al.* 2014; Labbé *et al.* 2015; More & Dumberry 2017; Dumberry & More 2020). While acceptable for the temperature, a 2-D approximation of magnetic fields is likely too restrictive, when compared to the complex geometry of the magnetic field in 3-D dynamo simulations (Schaeffer *et al.* 2017; Aubert 2019; Aubert *et al.* 2022).

In Jackson & Maffei (2020, hereafter referred to as Paper 1) we introduced an alternative columnar-flow formulation, called plesio-geostrophy (PG), that is designed to include the effect of magnetic fields in a fully 2-D framework that does not require severe assumptions on the geometry of the magnetic field. This is achieved by describing the Lorentz force only via a series of 2-D magnetic moments, derived via vertical integration of the original, 3-D magnetic field. The PG momentum equation is different from other columnar-flow implementations, and is designed to improve on the treatment of the magnetic effects at the CMB.

The original PG formulation (Paper 1) ignores the effect of thermal heterogeneities and of viscous mechanical boundary conditions. To include them in the PG equations is the goal of this study. The inclusion of these ingredients is essential in the development of a self-consistent model capable of simulating the decadal dynamics of Earth's core in geophysically realistic regimes. We further develop a framework for the numerical study of core dynamics, as governed by the PG equations. Our method of choice is a fully spectral, grid-free method, novel to the study of columnar thermal convection. In simple geometries, spectral strategies have been shown to be capable of superior convergence when compared to local approaches like finite differences (Boyd 2001). Our numerical approach allows us to implement both no-slip and stress-free mechanical boundary conditions, the latter not being commonly used in columnar-flow models. In presence of a solid interface, such as the CMB, no-slip conditions are strictly more appropriate. Stress-free boundaries, however, have been considered for computational reasons (Aubert *et al.* 2017; Aubert 2023). Within the columnar-flow community, only a weak-form description exists to include stress-free boundary conditions (Maffei *et al.* 2017), which involves considering an integrated version of the governing equations, such as an energy norm, as done in, for example, Zhang (1994). This approach is not well suited for numerical methodologies that are typically used since they aim at solving the governing equations themselves (i.e. the 'strong form').

The newly derived, hydrothermal PG system will be benchmarked against existing 3-D and columnar-flow methodologies by performing calculations of onset of thermal convection in a full sphere. The problem is a classical one, and has well known numerical (Chandrasekhar 1961; Jones *et al.* 2000; Zhang & Liao 2004, 2017; Zhang *et al.* 2007, 2017), low-E, asymptotic (Roberts 1965; Jones *et al.* 2000; Zhang & Liao 2004, 2017; Zhang *et al.* 2007, 2017) and columnar-flow solutions (Guervilly & Cardin 2016). The exact knowledge of onset values is a requisite when performing strongly forced simulations of thermal convection, which we will report on in a future publication.

The paper is structured as follows. In Section 2, we derive the mathematical modifications required to introduce thermally driven buoyancy in the PG momentum equation presented in Paper 1. Ignoring the effect of magnetic fields in the core, we present a system of equation that describes the evolution of columnar flows in presence of thermal anomalies in an internally heated fluid sphere. The spectral numerical methodology and the treatment of viscous boundary condition will be developed in Section 3. For the purposes of this paper, we focussed on the solution of eigenvalue problems, but the methodology can be extended to time-marching problems. In Section 4, we present the results of tests aimed at benchmarking the developments presented in Sections 2 and 3. In particular, we focus on validating some of the novel aspects of the PG set of equations (Section 4.1), on the calculation of reference solutions aimed at the onset of thermal convection at very low E (Section 4.2) and to the comparison of numerical results with existing 3-D and columnar-flow solutions (Section 4.3). We end the paper with a discussion, in Section 5.

2 DERIVATION OF THE PG THERMAL EQUATIONS

We consider a fully fluid sphere of radius r_o. To describe the physics within the sphere, we make use of both a cylindrical coordinate system (s, ϕ, z) and a spherical one (r, θ, ϕ). The centre of the sphere is defined as $s = z = 0$ and $r = 0$, respectively. The sphere rotates around a rotation axis aligned with the vertical direction $\hat{\mathbf{z}}$, at a rate Ω. The fluid inside the sphere is Boussinesq and characterized by constant values of thermal expansion coefficient α, kinematic viscosity ν, thermal diffusivity κ and reference density ρ_0. The fluid is subject to a radial gravitational field $\mathbf{g} = -\gamma\mathbf{r}$, where γ is a positive constant and $\mathbf{r}$ is the radial vector in spherical coordinates. We consider a reference state characterized by the fluid at rest and a conducting temperature profile characterized by $\nabla T_s = -\chi\mathbf{r}$, where χ is a positive constant, caused by a uniform distribution of internal volumetric heating in the sphere.

The non-dimensional equations describing the evolution of velocity, $\mathbf{u}$, temperature perturbation, T and dynamic pressure, p, are:

$$\frac{\partial \mathbf{u}}{\partial t} = -(\mathbf{u}\cdot\nabla)\mathbf{u} - 2\hat{\mathbf{z}}\times\mathbf{u} - \nabla p + RaE^2 T\mathbf{r} + E\nabla^2\mathbf{u} \tag{1}$$

$$\frac{\partial T}{\partial t} = -\mathbf{u}\cdot\nabla T + \frac{1}{Pr}\mathbf{u}\cdot\mathbf{r} + \frac{E}{Pr}\nabla^2 T \tag{2}$$

$$\nabla\cdot\mathbf{u} = 0, \tag{3}$$

where we introduced the Ekman, E, Rayleigh, Ra and Prantdl, Pr, numbers:

$$E = \frac{\nu}{\Omega r_o^2}, \quad Ra = \frac{\gamma\alpha\chi r_o^6}{\nu\kappa}, \quad Pr = \frac{\nu}{\kappa}. \tag{4}$$

In the above we non-dimensionalized measuring time in terms of the rotation timescale Ω^{-1}, length-scales in terms the core radius r_o, and temperature in terms of $\chi r_0^2 \nu\kappa^{-1}$. The non-dimensionalization adopted in this work is as in Zhang & Liao (2004, 2017), while the definitions of E, Ra and Pr (eq. 4) are the same as in Jones *et al.* (2000). This choice is not unique. Most notably, different authors adopt different definitions of Ra, E and of the non-dimensionalizations for time and temperature (Roberts 1968; Busse 1970; Jones *et al.* 2000; Zhang & Liao 2004; Guervilly & Cardin 2016; Zhang & Liao 2017), and indeed we used a different temperature scale in Paper 1 that lead to a different form of the Navier–Stokes equation and a different definition of the Rayleigh number. In thermal convection studies it is common to measure time in units of the viscous timescale r_0^2/ν (Jones *et al.* 2000; Guervilly & Cardin 2016), instead of the rotational timescale adopted in this work and in, for example Busse (1970) and Zhang & Liao (2004). We adopt the latter as it results in a non-dimensional momentum eq. (1) that allows to easily isolate inviscid dynamics by setting E to zero.

The governing eqs (1)–(3) are complemented with fixed-temperature:

$$T|_{r=1} = 0, \tag{5}$$

and non-penetration:

$$u_r|_{r=1} = 0, \tag{6}$$

boundary conditions. In the presence of viscosity additional mechanical boundary conditions are required. As is customary, we consider either no-slip:

$$u_\theta|_{r=1} = u_\phi|_{r=1} = 0, \tag{7}$$

or stress-free:

$$\frac{\partial}{\partial r}\left(\frac{u_\theta}{r}\right)\bigg|_{r=1} = \frac{\partial}{\partial r}\left(\frac{u_\phi}{r}\right)\bigg|_{r=1} = 0. \tag{8}$$

2.1 PG momentum equation

The columnar-flow approximation is implemented by making use of the following ansatz (Schaeffer & Cardin 2005a, b):

$$\mathbf{u}(s,\phi,z) = \frac{1}{H}\nabla\times(\Psi\hat{\mathbf{z}}) - \frac{sz}{H^2}u_s\hat{\mathbf{z}} = \frac{1}{sH}\frac{\partial\Psi}{\partial\phi}\hat{\mathbf{s}} - \frac{1}{H}\frac{\partial\Psi}{\partial s}\hat{\boldsymbol{\phi}} - \frac{z}{H^3}\frac{\partial\Psi}{\partial\phi}\hat{\mathbf{z}}, \tag{9}$$

where $\Psi(s,\phi)$ is a 2-D stream-function and $H = \sqrt{1-s^2}$ is the half-height of the sphere at a distance s from the rotation axis. The above ansatz results in incompressible flows satisfying non-penetration condition (eq. 6) at the outer boundary. That is, $u_r = 0$ at $r = 1$ or, equivalently, at $z = \pm H$. The prescription (eq. 9) is now the standard in columnar-flow formulations (Schaeffer & Cardin 2005a, b; Labbé *et al.* 2015; Schaeffer *et al.* 2016; Guervilly & Cardin 2016; Maffei *et al.* 2017; Guervilly *et al.* 2019; Gerick *et al.* 2020, 2021; Barrois *et al.* 2022). In the context of thermal convection, ansatz (eq. 9) has been corroborated by 3-D calculations. In fig. 5 of Gillet & Jones (2006) it is shown that in 3-D, asymptotic calculations both the $z-$independence of the horizontal flow and the linear $z-$dependence of the vertical velocity, are well justified at the onset of thermal convection. Furthermore, the 3-D numerical calculations of turbulent convection in a full sphere presented in Guervilly *et al.* (2019), illustrate that the horizontal flows show a remarkable degree of vertical invariance. In spherical shells, non-linear calculations show that thermal winds can partially disrupt the vertical invariance of the horizontal flows (Barrois *et al.* 2022), however, a high degree of columnarity is still observed outside the tangent cylinder.

To obtain an equation that describes the temporal evolution of Ψ we follow the PG methodology outlined in Paper 1. The main difference between the PG and other columnar-flow formulations lies in the order in which the differential and integration operations are applied to the momentum eq. (1). The common derivation (Cardin & Olson 1994) proceeds by first taking the curl of the momentum equation, which leads to the vorticity equation, in which the pressure gradient has been eliminated. The vertical component (i.e. the axial vorticity equation) is then integrated along the vertical direction. Introducing ansatz (eq. 9) in the resulting equation leads to an evolution equation for the stream-function Ψ (Schaeffer & Cardin 2005a, b). Within the PG framework, the vertical integration is taken before the curl operation. As shown in Paper 1, the rationale for doing so is to retain full control of surface terms arising from non-vanishing magnetic field contributions at the CMB.[1] Further manipulations are then required to eliminate pressure terms from the final equation. Eventually one obtains the following equation for the non-zonal (i.e. not-axysimmetric) velocity component:

$$\left[-\frac{\partial}{\partial s}\left(\frac{s}{H}\frac{\partial}{\partial s}\right)+\frac{1}{H}\left(\frac{\beta}{2}-\frac{1}{s}\right)\frac{\partial^2}{\partial\phi^2}\right]\frac{\partial\Psi}{\partial t}=\frac{s}{2H}\left(F_A+F_C+RaE^2F_T+EF_V\right). \tag{10}$$

The zonal component of the velocity is not considered in this study. In the above, $\beta = H^{-1}\mathrm{d}H/\mathrm{d}s = -s/H^2$ is the slope of the spherical boundary and the terms on the right-hand side are calculated from each term $\mathbf{f}$ (including inertia) appearing in the momentum eq. (1) via the following formula:

$$F=\frac{\mathrm{d}H}{\mathrm{d}s}\left[-2f_\phi|_0-\frac{1}{s}\frac{\partial}{\partial\phi}\widetilde{f}_z\right]+\hat{\mathbf{z}}\cdot\nabla\times[\overline{\mathbf{f}}_e], \tag{11}$$

where $f_\phi|_0$ denotes the ϕ component of $\mathbf{f}=\hat{\mathbf{s}}f_s+\hat{\boldsymbol{\phi}}f_\phi+\hat{\mathbf{z}}f_z$ evaluated at $z=0$ and $\mathbf{f}_e=\hat{\mathbf{s}}f_s+\hat{\boldsymbol{\phi}}f_\phi$ indicates its equatorial components. The overline and tilde operators denote, respectively the vertical, symmetric integral operator,

$$\overline{\Phi}=\int_{-H}^{H}\Phi\,\mathrm{d}z, \tag{12}$$

and the vertical, asymmetric integral operator,

$$\widetilde{\Phi}=\int_{-H}^{H}\mathrm{sgn}(z)\Phi\,\mathrm{d}z=\int_{0}^{H}\Phi\,\mathrm{d}z-\int_{-H}^{0}\Phi\,\mathrm{d}z, \tag{13}$$

where $\Phi(s,\phi,z)$ is a 3-D function, with general dependence on the vertical coordinate z, and $\mathrm{sgn}(z)$ is the sign of z: $\mathrm{sgn}(z)=1$ for $z>0$ and $\mathrm{sgn}(z)=-1$ for $z<0$. Throughout the paper, we also make use of the vertical averaging operation:

$$\langle\Phi\rangle=\frac{1}{2H}\int_{-H}^{H}\Phi\,\mathrm{d}z=\frac{1}{2H}\overline{\Phi}. \tag{14}$$

In eq. (10), F_A, F_C, F_T and F_V indicate the PG forcing derived from, respectively, the non-linear advection term, the Coriolis force, buoyancy and viscous dissipation. Note that the definition of these terms does not include the non-dimensional pre-factors, which appear explicitly in eq. (10). This is done to easily accommodate different pre-factors that arise from different non-dimensionalizations. The derivation that leads to the PG momentum eq. (10) results in the pressure term cancelling out, as desired (Paper 1).

Under non-penetration boundary conditions (eq. 6), the Coriolis term takes the following form:

$$F_C=-4\frac{s}{H}u_s, \tag{15}$$

while the viscous and advection terms are calculated directly via formula (11). For the viscous term, this gives:

$$F_V=\left\{\frac{\mathrm{d}H}{\mathrm{d}s}\left[-\frac{1}{s}\frac{\partial}{\partial\phi}\widetilde{(\nabla^2u_z)}-2(\nabla^2\mathbf{u})_\phi(0)\right]+\hat{\mathbf{z}}\cdot\nabla\times[\overline{(\nabla^2\mathbf{u})_e}]\right\}. \tag{16}$$

The latter term has a non-trivial structure when written in terms of Ψ that we do not give explicitly. Some mathematical manipulation aimed at simplifying the F_A and F_V terms are given in appendices A and B of Paper 1.

By replacing $\mathbf{f}=T\mathbf{r}$ in eq. (11) one readily obtains:

$$F_T=-\frac{1}{s}\frac{\partial}{\partial\phi}\left[\frac{\mathrm{d}H}{\mathrm{d}s}\widetilde{zT}+s\overline{T}\right] \tag{17}$$

and two new, 2-D variables emerge that describe the temperature field: $\widetilde{zT}$ and $\overline{T}$. Next, we consider these new thermal variables. Note that the quantity $\widetilde{zT}$ does not contain information on the equatorially antisymmetric temperature, because of the z factor. Using the definition (eq. 13) for the antisymmetric integration we obtain:

$$\widetilde{zT}=\int_{-H}^{H}\mathrm{sgn}(z)zT\,dz=\int_{-H}^{H}|z|T\,dz,$$

where $|z|=sgn(z)z$ denotes the absolute value of z. Therefore both $\widetilde{zT}$ and $\overline{T}$ are symmetric moments of the temperature field, but they weight the T contribution to the vertical integral differently along the vertical direction.

[1]Note the following mistakes in Paper 1: a sign error in the third terms of both lines in eq. (4.2); the factor $\cos\theta$ on the right-hand side of eq. (4.5) should be $\cos^{-1}\theta$.

2.2 PG thermal equations

Evolution equations for the thermal quantities $\overline{T}$ and $\widetilde{zT}$, introduced in the buoyancy term (eq. 17), can be derived from the 3-D temperature eq. (2). We briefly illustrate the derivation of the evolution equation for $\overline{T}$. Applying the symmetric integral operator eq. (12) to the temperature eq. (2) one obtains:

$$\frac{\partial \overline{T}}{\partial t} = -\int_{-H}^{H} \mathbf{u}\cdot\nabla T \, \mathrm{d}z + \frac{1}{Pr}\int_{-H}^{H} \mathbf{u}\cdot\mathbf{r} \, \mathrm{d}z + \frac{E}{Pr}\int_{-H}^{H} \nabla^2 T \, \mathrm{d}z.$$

The first two terms on the right-hand side can be manipulated thanks to the simple z dependence of $\mathbf{u}$ under the columnar-flow ansatz (eq. 9). In particular the advection term can be expanded as:

$$\begin{aligned}\int_{-H}^{H} \mathbf{u}\cdot\nabla T \, \mathrm{d}z &= \int_{-H}^{H}\left[u_s\frac{\partial T}{\partial s} + u_\phi\frac{1}{s}\frac{\partial T}{\partial \phi} + u_z\frac{\partial T}{\partial z}\right]\mathrm{d}z \\ &= u_s\int_{-H}^{H}\frac{\partial T}{\partial s}\,\mathrm{d}z + u_\phi\int_{-H}^{H}\frac{1}{s}\frac{\partial T}{\partial \phi}\,\mathrm{d}z - \frac{su_s}{H^2}\int_{-H}^{H} z\frac{\partial T}{\partial z}\,\mathrm{d}z. \end{aligned} \tag{18}$$

The first integral on the right-hand side is expanded using Leibniz integration rule:

$$\int_{-H}^{H}\frac{\partial T}{\partial s}\,dz = \frac{\partial}{\partial s}\int_{-H}^{H} T\,dz - \frac{dH}{ds}\left(T|_H + T|_{-H}\right) = \frac{\partial \overline{T}}{\partial s} + \frac{s}{H}\left(T|_H + T|_{-H}\right),$$

and the third one via integration by parts:

$$\int_{-H}^{H} z\frac{\partial T}{\partial z}\,dz = (zT)\,|_H - (zT)\,|_{-H} - \int_{-H}^{H} T\,dz = H\left(T|_H + T|_{-H}\right) - \overline{T}.$$

In the above, $T|_{\pm H}$ refers to the temperature fluctuation T, evaluated at the surface of the sphere, $z = \pm H$. Inserting these last two identities in eq. (18) we find that the surface terms cancel each other out. The advection terms therefore is entirely expressed as a function of $\mathbf{u}$ and $\overline{T}$:

$$\int_{-H}^{H} \mathbf{u}\cdot\nabla T\,dz = \mathbf{u}_e\cdot\nabla_e\overline{T} + \frac{su_s}{H^2}\overline{T}.$$

An evolution equation for $\widetilde{zT}$ is obtained applying the asymmetric integral operator (eq. 13) to the temperature eq. (2) and using manipulations similar to the ones illustrated above. Without further manipulating the diffusive terms, we obtain the following equations:

$$\frac{\partial \overline{T}}{\partial t} = -\mathbf{u}_e\cdot\nabla_e\overline{T} - \frac{su_s}{H^2}\overline{T} + \frac{1}{Pr}\frac{4}{3}sHu_s + \frac{E}{Pr}\overline{\nabla^2 T}, \tag{19}$$

$$\frac{\partial \widetilde{zT}}{\partial t} = -\mathbf{u}_e\cdot\nabla_e\widetilde{zT} - 2u_s\frac{s}{H^2}\widetilde{zT} + \frac{1}{Pr}\frac{1}{2}sH^2u_s + \frac{E}{Pr}\widetilde{z\nabla^2 T}, \tag{20}$$

where ∇_e is the component parallel to the equatorial plane. Note that no assumption on the geometry of the 3-D variable T have been made so far.

The diffusion terms can be expanded by use of Leibniz integration rule. For example, the term $\overline{\nabla^2 T}$ is:

$$\begin{aligned}\int_{-H}^{H}\nabla^2 T\,dz &= \int_{-H}^{H}\frac{1}{s}\frac{\partial}{\partial s}\left[s\frac{\partial T}{\partial s}\right]dz + \int_{-H}^{H}\frac{1}{s^2}\frac{\partial^2 T}{\partial \phi^2}\,dz + \int_{-H}^{H}\frac{\partial^2 T}{\partial z^2}\,dz \\ &= \frac{1}{s}\left[\frac{\partial}{\partial s}\int_{-H}^{H} s\frac{\partial T}{\partial s}\,dz - s\frac{dH}{ds}\left(\left.\frac{\partial T}{\partial s}\right|_H + \left.\frac{\partial T}{\partial s}\right|_{-H}\right)\right] \\ &\quad + \frac{1}{s^2}\frac{\partial^2 \overline{T}}{\partial \phi^2} + \left(\left.\frac{\partial T}{\partial z}\right|_H - \left.\frac{\partial T}{\partial z}\right|_{-H}\right) \\ &= \frac{1}{s}\left\{\frac{\partial}{\partial s}\left[s\frac{\partial \overline{T}}{\partial s} - s\frac{dH}{ds}\left(T|_H + T|_{-H}\right)\right] - s\frac{dH}{ds}\left(\left.\frac{\partial T}{\partial s}\right|_H + \left.\frac{\partial T}{\partial s}\right|_{-H}\right)\right\} \\ &\quad + \frac{1}{s^2}\frac{\partial^2 \overline{T}}{\partial \phi^2} + \left(\left.\frac{\partial T}{\partial z}\right|_H - \left.\frac{\partial T}{\partial z}\right|_{-H}\right) \\ &= \frac{1}{s}\frac{\partial}{\partial s}\left[s\frac{\partial \overline{T}}{\partial s}\right] - \frac{1}{s}\frac{\partial}{\partial s}\left[s\frac{dH}{ds}\left(T|_H + T|_{-H}\right)\right] - \frac{dH}{ds}\left(\left.\frac{\partial T}{\partial s}\right|_H + \left.\frac{\partial T}{\partial s}\right|_{-H}\right) \\ &\quad + \frac{1}{s^2}\frac{\partial^2 \overline{T}}{\partial \phi^2} + \left(\left.\frac{\partial T}{\partial z}\right|_H - \left.\frac{\partial T}{\partial z}\right|_{-H}\right)\end{aligned}$$

By collecting the derivatives of the variable $\overline{T}$ and by recognising that:

$$-\frac{dH}{ds}\left(\left.\frac{\partial T}{\partial s}\right|_H + \left.\frac{\partial T}{\partial s}\right|_{-H}\right) + \left(\left.\frac{\partial T}{\partial z}\right|_H - \left.\frac{\partial T}{\partial z}\right|_{-H}\right) = \frac{1}{H}\left(\left.\frac{\partial T}{\partial r}\right|_H + \left.\frac{\partial T}{\partial r}\right|_{-H}\right),$$

we obtain the following:

$$\overline{\nabla^2 T} = \nabla_e^2 \overline{T} - \frac{1}{s}\frac{\partial}{\partial s}\left[s\frac{dH}{ds}(T|_H + T|_{-H})\right] + \frac{1}{H}\left(\left.\frac{\partial T}{\partial r}\right|_H + \left.\frac{\partial T}{\partial r}\right|_{-H}\right).$$

Similar manipulations lead to the following form for the diffusive term in eq. (20):

$$\widetilde{z\nabla^2 T} = \nabla_e^2 \widetilde{zT} + \frac{1}{s}\frac{\partial}{\partial s}\left[s^2(T|_H + T|_{-H})\right] + \left(\left.\frac{\partial T}{\partial r}\right|_H + \left.\frac{\partial T}{\partial r}\right|_{-H}\right) + 2T|_0 - (T|_H + T|_{-H}).$$

Therefore, the diffusion terms in the above equations are not closed in the $\overline{T}$ and $\widetilde{zT}$ variables, and an approximate form needs to be found. We use the following argument: given the columnar nature of the flow, we expect the vertical variations in temperature to be weak compared to the equatorial ones. We therefore assume that the vertically averaged Laplacian of temperature to be well approximated by the Laplacian of the vertically averaged temperature:

$$\langle \nabla^2 T\rangle \simeq \nabla_e^2 \langle T\rangle. \tag{21}$$

Note that eq. (21) is a strict equality if T is a 2-D variable, with no vertical dependence. Substituting eq. (14) in eq. (21) leads to the following approximate form:

$$\overline{\nabla^2 T} \simeq H\nabla_e^2\left(\frac{\overline{T}}{H}\right) \tag{22}$$

A similar argument for $\widetilde{z\nabla^2 T}$ is less rigorous, but assuming that the temperature has weak variations along the vertical direction, and using eq. (13), yields the following:

$$\widetilde{z\nabla^2 T} \simeq H^2\nabla_e^2\left(\frac{\widetilde{zT}}{H^2}\right). \tag{23}$$

We therefore use eq. (22) and eq. (23) to approximate the diffusive terms in eqs (19) and (20). The validity of these approximations is assessed in Section 4.1.2. Note that, intuitively, it is tempting to approximate the diffusion terms as $\overline{\nabla^2 T} \simeq \nabla^2 \overline{T}$ and $\widetilde{z\nabla^2 T} \simeq \nabla^2 \widetilde{zT}$. However, as we show in Section 4.1.2, these aesthetically appealing substitution results in pathological behaviour at $s = 1$.

2.3 Linearized equations

In the remainder of the paper we focus our attention on the solution to the linearized version of the PG equations derived above. In particular we consider small perturbations around a background state defined by a fluid at rest and a conductive thermal gradient. By neglecting non-linear terms in the PG eqs (10), (19) and (20) we obtain the linearized system:

$$\left[-\frac{\partial}{\partial s}\left(\frac{s}{H}\frac{\partial}{\partial s}\right) + \frac{1}{H}\left(\frac{\beta}{2} - \frac{1}{s}\right)\frac{\partial^2}{\partial\phi^2}\right]\frac{\partial\Psi}{\partial t} = \frac{s}{2H}\left(F_C + RaE^2F_T + EF_V\right), \tag{24}$$

$$\frac{\partial\overline{T}}{\partial t} = \frac{1}{Pr}\frac{4}{3}sHu_s + \frac{E}{Pr}H\nabla_e^2\left(\frac{\overline{T}}{H}\right), \tag{25}$$

$$\frac{\partial\widetilde{zT}}{\partial t} = \frac{1}{Pr}\frac{1}{2}sH^2u_s + \frac{E}{Pr}H^2\nabla_e^2\left(\frac{\widetilde{zT}}{H^2}\right). \tag{26}$$

In the above we made use of the approximations (22) and (23).

Non-penetration (eq. 6) and fixed-temperature (eq. 5) require the following boundary conditions at $s = 1$:

$$\Psi|_{s=1} = \overline{T}\big|_{s=1} = \widetilde{zT}\big|_{s=1} = 0. \tag{27}$$

Stress-free or no-slip boundary conditions are implemented as detailed in Section 3.3. Finally, we require regularity at the origin of the coordinate system, $s = 0$ (Lewis & Bellan 1990).

3 NUMERICAL METHOD

3.1 Variables expansion

To solve the linear system (24)–(26), we use the following expansion to describe the spatio-temporal evolution of Ψ, $\overline{T}$ and $\widetilde{zT}$:

$$\Psi(s,\phi,t) = \sum_{j=1}^{N} c_j^m\ \Psi_j^m(s)\mathrm{e}^{\mathrm{i}m\phi+\lambda t}, \tag{28}$$

$$\overline{T}(s,\phi,t) = \sum_{j=1}^{N} \overline{a}_j^m\ \overline{T}_j^m(s)\mathrm{e}^{\mathrm{i}m\phi+\lambda t}, \tag{29}$$

$$\widetilde{zT}(s,\phi,t) = \sum_{j=1}^{N} \widetilde{a}_j^m \, \widetilde{zT}_j^m(s) \mathrm{e}^{\mathrm{i}m\phi+\lambda t}. \tag{30}$$

In the above, m is the azimuthal wavenumber, c_j^m, $\overline{a}_j^m$, $\widetilde{a}_j^m$, are the expansion coefficients, and N is the maximum values for j considered in the expansion. Given the linear nature of eqs (24)–(26), the problem is decoupled in the azimuthal wavenumber and there is no need to consider a sum over m in expansions (28)–(30).

The radial functions $\Psi_j^m(s)$, $\overline{T}_j^m(s)$ and $\widetilde{zT}_j^m(s)$ are defined as follows

$$\Psi_j^m(s) = s^m H^3 P_{j-1}^{(3/2,m)}(2s^2-1). \tag{31}$$

$$\overline{T}_j^m(s) = s^m H^3 P_{j-1}^{(3,m-1/2)}(2s^2-1), \tag{32}$$

$$\widetilde{zT}_j^m(s) = s^m H^4 P_{j-1}^{(4,m-1/2)}(2s^2-1), \tag{33}$$

where $P^{(\alpha,\beta)}$ are Jacobi polynomials. The above definitions satisfies boundary conditions (27) and regularity at the origin. The specific α and β parameters of the Jacobi polynomials $P^{(\alpha,\beta)}$ are chosen so that the radial basis satisfy the following orthogonality conditions:

$$\int_0^1 \Psi_i^m(s)\Psi_j^m(s)\frac{s}{H^3}\mathrm{d}s \propto \delta_{ij} \tag{34}$$

$$\int_0^1 \overline{T}_i^m(s)\overline{T}_j^m(s)\mathrm{d}s \sim \int_0^1 \widetilde{zT}_i^m(s)\widetilde{zT}_j^m(s)\mathrm{d}s \propto \delta_{ij}, \tag{35}$$

with proportionality factors that can be calculated from the orthogonality relationships of the Jacobi polynomials.

The stream-function expansion (31) is motivated by the solution to the inviscid inertial-wave eigenvalue problem, obtained by inserting eq. (28) in the linear eq. (24), and setting $Ra = E = 0$. The resulting problem has an analytical solution (Paper 1) described by the eigenmodes (eq. 31) with eigenvalues:

$$\lambda_j^m = \mathrm{i}\omega_j^m = -\mathrm{i}\frac{m}{j(2j+2m+1)+m/2+m^2/4}. \tag{36}$$

These inertial modes form a complete basis set and satisfy the first of orthogonality conditions (eq. 34). Note that for other columnar-flow models the solution to the inviscid inertial-mode problem is still defined by eq. (31), but the eigenvalues have a different expression depending on the implementation (Maffei *et al.* 2017).

3.2 Matrix–vector formulation

A set of equations for the coefficients c_j^m, $\overline{a}_j^m$, $\widetilde{a}_j^m$ is obtained by considering the weak form of eqs (24)–(26). The weak form of a differential equation can be constructed by multiplying the original form of the equation (its 'strong form') by a chosen test function and integrating in space (see Chaskalovic & Chaskalovic 2008, chapter 1). For example, in Zhang (1994, 1995), Zhang & Liao (2004) and Zhang *et al.* (2007) the strong form of the momentum eq. (1) is multiplied by the complex conjugate of the velocity field itself, $\mathbf{u}^*$. Note that the coefficients c_j^m, $\overline{a}_j^m$, $\widetilde{a}_j^m$ could be found via a collocation method (as done in e.g. Barrois *et al.* 2022), rather than a weak-form approach. The advantage of using the latter, also called 'variational' approach, is the ability to implement no-slip or stress-free boundary conditions in an asymptotic sense, allowing to find a velocity solution that is the sum of the inviscid solution plus a small viscous perturbation (Zhang 1994, 1995; Zhang & Liao 2004; Zhang *et al.* 2007; Maffei *et al.* 2017). In our case, the weak-form approach also allows us to consider the stress-free condition over the entirety of the spherical boundary (see Section 3.3.2). Conversely, considering the strong form of the PG momentum equation (eq. 10), would allow to apply the stress-free condition only on the $s = 1$ boundary of the equatorial disc. We obtain the weak-form version of the PG equations by inserting expansions (28)–(30) in the linear eqs (24)–(26) and by multiplying the resulting equations by the complex conjugate of, respectively $\Psi_i^m(s)\mathrm{e}^{\mathrm{i}m\phi}$, $\overline{T}_i^m(s)\mathrm{e}^{\mathrm{i}m\phi}$ and $\widetilde{zT}_i^m(s)\mathrm{e}^{\mathrm{i}m\phi}$. Upon integration over the equatorial disk in s and ϕ we obtain a set of equations that can be succinctly written in the following matrix form:

$$\lambda\boldsymbol{\mathcal{N}}\cdot\mathbf{c} = (\boldsymbol{\Sigma}+E\boldsymbol{\mathcal{G}})\cdot\mathbf{c} + Ra\,E^2\left(\overline{\boldsymbol{\mathcal{B}}}\cdot\overline{\mathbf{a}}+\widetilde{\boldsymbol{\mathcal{B}}}\cdot\widetilde{\mathbf{a}}\right), \tag{37}$$

$$\lambda\overline{\boldsymbol{\mathcal{C}}}\cdot\overline{\mathbf{a}} = \frac{1}{Pr}\overline{\boldsymbol{\mathcal{R}}}\cdot\mathbf{c} + \frac{E}{Pr}\overline{\boldsymbol{\mathcal{M}}}\cdot\overline{\mathbf{a}}, \tag{38}$$

$$\lambda\widetilde{\boldsymbol{\mathcal{C}}}\cdot\widetilde{\mathbf{a}} = \frac{1}{Pr}\widetilde{\boldsymbol{\mathcal{R}}}\cdot\mathbf{c} + \frac{E}{Pr}\boldsymbol{\mathcal{M}}\cdot\widetilde{\mathbf{a}}. \tag{39}$$

In the above, $\mathbf{c}$, $\overline{\mathbf{a}}$ and $\widetilde{\mathbf{a}}$ are 1-D arrays containing the coefficients $c_j^m(t)$, $\overline{a}_j^m(t)$ and $\widetilde{a}_j^m(t)$; $\boldsymbol{\mathcal{N}}$, $\overline{\boldsymbol{\mathcal{C}}}$ and $\widetilde{\boldsymbol{\mathcal{C}}}$ are the left-hand side mass matrices; $\boldsymbol{\Sigma}$ is the Coriolis matrix and $\boldsymbol{\mathcal{G}}$ is the viscosity matrix; $\overline{\boldsymbol{\mathcal{B}}}$ and $\widetilde{\boldsymbol{\mathcal{B}}}$ are the buoyancy matrices; $\overline{\boldsymbol{\mathcal{R}}}$ and $\widetilde{\boldsymbol{\mathcal{R}}}$ are the thermal advection matrices; $\overline{\boldsymbol{\mathcal{M}}}$ and $\widetilde{\boldsymbol{\mathcal{M}}}$ are the thermal diffusion matrices. We discuss below the form of each of these matrices.

Under proper normalization of the basis functions (eqs 31–33) the mass matrices $\boldsymbol{\mathcal{N}}$, $\overline{\boldsymbol{\mathcal{C}}}$ and $\widetilde{\boldsymbol{\mathcal{C}}}$ are all equal to a unit matrix of size $N \times N$. For the $\overline{\boldsymbol{\mathcal{C}}}$ and $\widetilde{\boldsymbol{\mathcal{C}}}$ this simply follows from the orthogonality relations (eq. 35); the orthogonality of the matrix $\boldsymbol{\mathcal{N}}$ follows from recognizing that

the normal mode solution eqs (31)–(36) satisfies the following equation:

$$\lambda_j^m \left[-\frac{d}{\mathrm{d}s}\left(\frac{s}{H}\frac{d}{\mathrm{d}s}\right) - \frac{1}{H}\left(\frac{\beta}{2} - \frac{1}{s}\right) m^2 \right] \Psi_j^m(s) = \frac{s}{2H}(F_C)_j^m = -\mathrm{i}m\frac{2s}{H^3}\Psi_j^m(s), \tag{40}$$

so that the orthogonality eq. (34) implies orthogonality of the mass term via:

$$\begin{aligned}\mathcal{N}_{ij} &= \int_0^{2\pi}\int_0^1 \Psi_i^m(s)\left[-\frac{d}{ds}\left(\frac{s}{H}\frac{d}{ds}\right) - \frac{1}{H}\left(\frac{\beta}{2} - \frac{1}{s}\right) m^2 \right] \Psi_j^m(s)\, ds\, d\phi \\ &= -\frac{2\mathrm{i}m}{\lambda_j^m}\int_0^{2\pi}\int_0^1 \Psi_i^m(s)\frac{s}{H^3}\Psi_j^m(s)\, ds\, d\phi = \frac{1}{\lambda_j^m}\Sigma_{ij}^{np}.\end{aligned}$$

Noting definition eq. (17) of the buoyancy term F_T, the buoyancy matrices $\overline{\mathcal{B}}$ and $\widetilde{\mathcal{B}}$ have the following shape:

$$\begin{aligned}\overline{\mathcal{B}}_{ij} &= -\int_0^{2\pi}\int_0^1 \mathrm{i}m\Psi_i^m(s)\frac{s}{2H}\overline{T}_j^m(s)\; ds d\phi, \\ \widetilde{\mathcal{B}}_{ij} &= \int_0^{2\pi}\int_0^1 \mathrm{i}m\Psi_i^m(s)\frac{s}{2H^2}z\widetilde{T}_j^m(s)\; ds d\phi.\end{aligned}$$

The entries of the thermal matrices $\overline{\mathcal{R}}$, $\widetilde{\mathcal{R}}$, $\overline{\mathcal{M}}$ and $\widetilde{\mathcal{M}}$ are obtained in a similar fashion.

Finally, the entries of the $\mathbf{\Sigma}$ and $\mathcal{G}$ depends on whether we consider no-slip or stress-free boundary conditions and is consider in the next Section.

3.3 Viscous boundary conditions

So far we have only considered non-penetration of the flow at the boundary of the sphere. In the presence of viscosity, additional mechanical boundary conditions are needed. In particular, we consider either no-slip (eq. 7) or stress-free (eq. 8). In either case, we cannot directly apply the conditions on the velocity field (eq. 9), since a condition applied on $z = \pm H$ will propagate along the entire fluid column. The result would be a too restrictive description of the flows allowed in the domain. As was done in Maffei *et al.* (2017), we assume that flows in the bulk of the domain are represented via eq. (9) and that small viscous corrections can be parametrized via the inclusion of thin boundary layers that develop in the presence of viscosity. In both cases the total velocity field, $\mathbf{v}$ is expanded as:

$$\mathbf{v} = \mathbf{u} + \mathbf{u}_1, \tag{41}$$

where $\mathbf{u}$ is the interior flow described via the columnar flow formalism (eq. 9) and satisfying only non-penetration condition (eq. 6) at the boundary and $\mathbf{u}_1$ is a correction that ensures that the total flow satisfies eq. (7) or eq. (8) through the development of viscous boundary layers. For low values of E, it is expected that $||\mathbf{u}_1|| \ll ||\mathbf{u}||$ in the interior of the domain (where $||\mathbf{u}||$ indicates the L_2 norm of the vector $\mathbf{u}$). Within the boundary layers, $||\mathbf{u}_1|| \simeq ||\mathbf{u}||$ and $\mathbf{u}_1$ has generally a non-columnar structure. Its effect on the columnar flows $\mathbf{u}$, however, can be described by correction terms, proportional to E in the stress-free case (see for example Liao *et al.* 2001) and $E^{1/2}$ in the no-slip case (see for example Kudlick 1966), that can be expressed entirely as a function of the interior, columnar flow $\mathbf{u}$.

3.3.1 *No-slip condition*

No-slip correction factors can be derived by neglecting the effect of buoyancy and non-linear advection terms in the momentum eq. (1). When all velocity components vanish at the CMB (eq. 7) the interior flow, of the form (eq. 9), must be matched to a boundary layer flow that is only significant in a thin layer, the thickness of which is proportional to $E^{1/2}$. A secondary interior flow is then induced, the leading order of which is a radial flow called Ekman pumping (Greenspan 1968). In the case of columnar flows, the Ekman pumping takes the following form [see appendix C in Schaeffer (2004)]:

$$u_{1r}|_{\pm H} = \frac{E^{1/2}}{2\sqrt{H}}\left[-\frac{s}{2H}u_\phi - \frac{5}{2}\frac{s}{H^2}u_s - H\left(\omega_z - \frac{s}{H^2}\frac{\partial u_s}{\partial \phi}\right)\right], \tag{42}$$

where $\omega_z = \hat{\mathbf{z}}\cdot\nabla\times\mathbf{u}$ is the axial vorticity and the velocity components $(u_s.u_\phi, u_z)$ above are defined via the columnar flow ansatz (eq. 9). Note that this definition is strictly valid for low-frequency motions. This simplifying assumption is justified by noting that the oscillation frequency of hydrodynamic, quasi-geostrophic inertial motions is the lowest among all the possible 3-D solutions (Zhang *et al.* 2001). The Ekman pumping correction (eq. 42) is widely used in the columnar-flow literature (e.g. Schaeffer & Cardin 2005a, b; Guervilly & Cardin 2016; Guervilly *et al.* 2019; Barrois *et al.* 2022) and it is typically adopted to model boundary terms arising from the vertically averaging procedure of the momentum equation. Here we follow an analogous methodology and specialize it to our PG formulation. We apply formula (11) with $\mathbf{f} = -2\hat{\mathbf{z}}\times\mathbf{v}$, where $\mathbf{v}$ is the total flow (eq. 41). Without assuming a columnar shape for $\mathbf{v}$ and relaxing the non-penetration boundary condition (eq. 6), the Coriolis term takes the following, general form:

$$F_C = -4\frac{s}{H}v_s|_0 + \frac{2}{H}\left(v_r|_H + v_r|_{-H}\right). \tag{43}$$

The details of the derivation can be found in Appendix A. Given that, in the interior $\mathbf{v} \simeq \mathbf{u}$ and that $u_r|_{\pm H} = 0$, we finally obtain:

$$F_C = -4\frac{s}{H}u_s + \frac{2}{H}\left(u_{1r}|_H + u_{1r}|_{-H}\right), \tag{44}$$

where $u_{1r}|_{\pm H}$ is given by formula (42). The second term of the above definition constitutes the correction factor for the no-slip boundary conditions, and it is proportional to $E^{1/2}$, as expected.

The viscous term, F_V, under no-slip conditions is given by the form (eq. 16), directly calculated from the interior flow $\mathbf{u}$.

Inserting eqs (44) and (16) in the momentum eq. (24) and forming its weak-form version eq. (37), we find that:

$$\boldsymbol{\Sigma} = \boldsymbol{\Sigma}^{np} + E^{1/2}\boldsymbol{\Sigma}^{ns},$$
$$\boldsymbol{\mathcal{G}} = \boldsymbol{\mathcal{G}}^{np}.$$

In the above:

$$\Sigma_{ij}^{np} = -2\mathrm{i}m\int_0^{2\pi}\int_0^1 \Psi_i^m(s)\frac{s}{H^3}\Psi_j^m(s)\,\mathrm{d}s\,\mathrm{d}\phi, \tag{45}$$

$$E^{1/2}\Sigma_{ij}^{ns} = \int_0^{2\pi}\int_0^1 \Psi_i^m(s)\mathrm{e}^{-\mathrm{i}m\phi}\frac{s}{H^2}\left(u_{1r}|_H + u_{1r}|_{-H}\right)_j^m\,\mathrm{d}s\,\mathrm{d}\phi, \tag{46}$$

$$\mathcal{G}_{ij}^{np} = \int_0^{2\pi}\int_0^1 \Psi_i^m(s)\mathrm{e}^{-\mathrm{i}m\phi}\frac{s}{2H}(F_V)_j^m\;\mathrm{d}s\mathrm{d}\phi, \tag{47}$$

The superscripts np indicates integrals obtained by considering non-penetration boundary conditions alone, and ns refers to integrals specific to the no-slip parametrizations.

Note that the Ekman pumping term $u_{1r}|_{\pm H}$ has a singular behaviour at $s = 1$, with a singularity that behaves as $H^{-3/2}$ (see Appendix B). The physical reason behind this singularity is that the Ekman pumping flow (eq. 42) is strictly valid for zero-frequency motions, for which the boundary layer has a singularity at $s = 1$ (Greenspan 1968). In columnar-flow models, this singularity worsens when eq. (42) is inserted in the momentum equation. For our PG model, this results in a singularity that scales as $H^{-5/2}$ (see eq. 44). In the majority of columnar-flow models that use eq. (42) to parametrize no-slip boundary conditions (Schaeffer 2004; Schaeffer & Cardin 2005a, b; Guervilly & Cardin 2016; Guervilly *et al.* 2019), the momentum equation is discretized via a local method (e.g. finite difference) and the singularity in $s = 1$ is avoided by not explicitly solving for the momentum equation there. This however introduces some ambiguity as the location of the outermost radial point is somewhat arbitrary.

The weak-form approach used here, under which the expansion coefficients $\mathbf{c}$, $\overline{\mathbf{a}}$ and $\widetilde{\mathbf{a}}$ are found by integration of the PG equations, allows us to quench the singularity at $s = 1$, stemming from the Ekman pumping term (eq. 42). It is indeed possible to show that the integrand involved in eq. (46) now contains a $H^{-1/2}$ behaviour (see Appendix B). Although in itself this would still be singular in $s = 1$, it is an integrable singularity, and therefore there is no fundamental issue with calculating the matrix $\boldsymbol{\Sigma}^{ns}$. Namely, we do not need to explicitly exclude the $s = 1$ point in order to calculate the integrals in eq. (46).

3.3.2 *Stress-free condition*

Following Zhang (1994) and Maffei *et al.* (2017), we implement the stress-free boundary condition (eq. 8) in a weak-form sense. Consider the viscous matrix $\boldsymbol{\mathcal{G}}$ from eq. (37). Dropping the indices i and j for ease of notation, its entries are:

$$\mathcal{G} = \int_{disc}\Psi^*\frac{s}{2H}F_V\;\mathrm{d}s\mathrm{d}\phi. \tag{48}$$

The above integral can be modified so that the stress-free condition is explicitly taken into account, via manipulations detailed in Appendix C. The final result is:

$$\begin{aligned}\mathcal{G} = \mathcal{G}^{sf} = &-\int_{core}\nabla\times\mathbf{U}^*\cdot\nabla\times\mathbf{u}\,\mathrm{d}V + 2\oint_{CMB}(U_\theta^* u_\theta + U_\phi^* u_\phi)\,\mathrm{d}\Omega\\ &+\oint_{CMB}\left\{-\frac{\omega_r}{\sin\theta}\frac{\partial}{\partial\theta}\left[\Psi^*\frac{1}{2}\frac{\sin^2\theta}{|\cos\theta|}\right] + \Psi^*|\tan\theta|\left[\frac{1}{2}\frac{\partial^2 u_\phi}{\partial r^2} - \frac{1}{2\sin\theta}\frac{\partial}{\partial r}\left(\frac{1}{r}\frac{\partial u_r}{\partial\phi}\right) + u_\phi\right]\right\}\mathrm{d}\Omega,\end{aligned} \tag{49}$$

where $\omega_r = \hat{\mathbf{r}}\cdot\nabla\times\mathbf{u}$ is the radial component of the vorticity, $\mathrm{d}V = s\mathrm{d}\phi\mathrm{d}s\mathrm{d}z$ is the infinitesimal volume element and $\mathrm{d}\Omega = \sin\theta d\theta\mathrm{d}\phi$ is the infinitesimal surface element on the spherical CMB surface, and

$$\mathbf{U}^* = \nabla\times\left[\frac{1}{2H}\Psi^*\hat{\boldsymbol{z}}\right] - \frac{\partial\Psi^*}{\partial\phi}\frac{1}{2H^2}\mathrm{sgn}(z)\hat{\boldsymbol{z}} \tag{50}$$

is a pseudo velocity field introduced to make the above integrals easier to parse. In the above, the volume integrals are taken over the entire, 3-D spherical domain, while the surface integrals are taken on the outer surface alone (the CMB).

The matrices $\boldsymbol{\Sigma}$ and $\boldsymbol{\mathcal{G}}$ in the stress-free cases are the obtained via eq. (15) and formula (49):

$$\boldsymbol{\Sigma} = \boldsymbol{\Sigma}^{np}$$
$$\boldsymbol{\mathcal{G}} = \boldsymbol{\mathcal{G}}^{sf},$$

where the matrix $\mathbf{\Sigma}^{np}$ is as defined in eq. (45) and the elements $\mathcal{G}_{ij}^{sf}$ (where the superscript sf denotes 'stress-free') are obtained replacing $\Psi^* = \Psi_i^m(s)\mathrm{e}^{-\mathrm{i}m\phi}$ and $\Psi = \Psi_j^m(s)\mathrm{e}^{\mathrm{i}m\phi}$ in eqs (49) and (50).

Note that by expanding the velocity field in terms of inertial modes, we obtain a formulation that is similar to that of Zhang & Liao (2004), in which it is assumed that the solution at the onset of thermal convection is given by a superposition of quasi-geostrophic inertial modes (QGIW), first calculated analytically in Zhang *et al.* (2001). The use of the weak formalism, under which the governing equations are projected upon the appropriate velocity and temperature basis, is another similarity with Zhang & Liao (2004), which allows for the calculation of the stress-free integral (eq. 49). One important difference with our methodology lies in the columnar prescription (eq. 9), which describes a different behaviour in z than the 3-D, QGIW basis adopted in Zhang & Liao (2004), as detailed in Maffei *et al.* (2017). Namely, while the equatorial components of eq. (31) have no vertical variation, the same is not true for the QGIW solutions, although their vertical complexity is the lowest amongst all the allowed 3-D solutions (Zhang *et al.* 2001). The difference stems from the fact that the QGIW modes are a solution to the unapproximated, 3-D momentum eq. (1) (upon setting $Ra = 0$), whereas the PG, and other columnar-flow solutions, impose a more restrictive behaviour in z as a starting ansatz.

3.4 Gauss quadrature and numerical implementation

All elements of the matrices defined in the previous Section involve integrals in the cylindrical radial, s, and azimuthal, ϕ, directions. The latter are trivially handled as the ϕ dependence in the integrands simplifies as a result of the linear nature of the PG eqs (24)–(26) considered here. The integrals in the s direction are calculated numerically via Gauss quadrature. For analogous 3-D, spherical calculations, it is customary to use Gauss-Legendre quadrature in the latitudinal, θ, direction and Gauss–Chebyshev in the radial, r direction (Li *et al.* 2010; Marti *et al.* 2014; Lin *et al.* 2016), since the quadrature nodes and weights are easily computed. Here we use the more general Gauss-Jacobi quadrature rule. The main reason for this choice comes from the analysis of the no-slip matrix $\mathbf{\Sigma}^{ns}$. Given definition (eq. 9) and our choice of the basis functions (eq. 31), it can be shown (see Appendix B) that the integrand in Σ_{ij}^{ns} above contains a sum of terms proportional to half-integer powers of H. Conversely, the other integrals involved in eq. (37) only contain integer powers in s and H, for example:

$$\Sigma_{ij}^{np} = -4\mathrm{i}m\pi \int_0^1 s^{2m+1} H^3 P_{i-1}^{(3/2,m)}(2s^2-1) P_{j-1}^{(3/2,m)}(2s^2-1)\,\mathrm{d}s. \tag{51}$$

While Σ_{ij}^{np} is amenable to Gauss–Chebyshev integration, Σ_{ij}^{ns} is not. Multiplying the momentum eq. (24) by an integration weight to render Σ_{ij}^{ns} integrable via Gauss–Chebyshev quadrature, would only transfer the problem to the other terms in eq. (37). Gauss–Jacobi quadrature can treat the different non-polynomial pre-factors in the integrands involved by treating them as integration weights. The Gauss–Jacobi quadrature rule states that, for $f(x)$ a polynomial in x of degree $2N+1$, the formula

$$\int_{-1}^{1} (1-x)^\alpha (1+x)^\beta f(x)dx = \sum_{l=1}^{N} w_l f(x_l), \tag{52}$$

where $\alpha, \beta > -1$, is exact if x_l are chosen to be the zeros of $P_{N+1}^{(\alpha,\beta)}$ and w_l are quadrature weights, calculated via well-known formulae (e.g. chapter 8 of Hildebrand 1987). We perform the substitution $x = 2s^2 - 1$ for all integrals in s involved in eqs (37)–(39), and transform them into the form required by eq. (52). In our case, α and β are rational numbers. The Gauss–Chebyshev rule is retrieved for $\alpha = \beta = \pm 1/2$, which is not the case for our calculations, nor can this condition be trivially met, for all terms in all equations, by choosing integration weights. For the integrals we obtain, such as eq. (51), α is half of the exponent with which H can be collected in the integrand, and β is proportional to m. For the specific case of eq. (51), $\alpha = 3/2$, $\beta = m$. As we show in Appendix B, the no-slip term Σ_{ij}^{ns} requires the application of Gauss-Jacobi rules with $\beta = m$ and $\alpha = \pm 1/4; 3/4$ and $\beta = m$, which are incompatible with the quadrature rule obtained for eq. (51). Therefore different quadrature rules have been used for different integrals.

The disadvantage of Gauss–Jacobi quadrature is that no closed-form solution exists (to our knowledge) for the zeros, x_l and weights, w_l, and they have to be determined numerically.

The procedure outline above is implemented in `Wolfram Mathematica` (version 12.3.1.0). The radial derivatives of the basis eqs (31)–(33), involved in the calculation of the various terms in eqs (24)–(26), are calculated symbolically. The Gauss–Jacobi quadrature nodes and weights are calculated numerically at arbitrary precision. All calculations involved in the production of the results shown in the next Section are performed at least at machine precision. Experimentally we found that accurate results are obtained by setting the precision (which in `Mathematica` is the number of digits used to represent numbers) equal to N, the maximum degree in the radial expansions (28)–(30). The matrices were computed in parallel on ETH's supercomputer Euler.

The problem of finding the critical Ra value for the onset of thermal convection can be formulated as a coupled eigenvalue-optimization problem. For fixed E, Pr, Ra and m the eigenvalue problem (eqs 37–39) has a solution for which the real part of λ (i.e. the growth rate) is maximum. This is the most unstable mode and we need to find the Ra value for which $\mathrm{Re}\{\lambda\} = 0$ (up to a certain numerically acceptable tolerance). This gives the value $Ra_{c,m}$, above which perturbations at the chosen m grow as a result of thermal convection. The critical value for the onset of thermal convection at the given E, Pr is $Ra_c = \min_m\{Ra_{c,m}\}$. That is, we need to find the critical azimuthal wavenumber m_c for which the convective instability is characterized by the lowest value of Ra. At onset $\mathrm{Im}\{\lambda\} = \omega_c$ defines the drift frequency of the solution.

Table 1. 3-D onset of thermal convection calculations performed with `QuICC`, for both no-slip and stress-free boundaries. In the table we report the E and Pr combinations for the calculations, the resulting critical parameters Ra_c, ω_c and m_c, and the resolution N_r and L, indicating the spectral truncation of, respectively, the radial and latitudinal expansions representing the solution (see Section 3.5). The resolution is reported for transparency, and does not correspond to an accurate estimate of the minimal values for N_r and L at convergence.

E	Pr	Ra_c	ω_c	m_c	N_r	L
		No-slip				
5×10^{-4}	0.1	1.589×10^5	-0.1213	3	64	64
1×10^{-4}	0.1	9.642×10^5	-0.07855	5	128	128
5×10^{-5}	0.1	2.304×10^6	-0.06354	6	128	128
1×10^{-5}	0.1	1.688×10^7	-0.04025	11	128	128
5×10^{-6}	0.1	4.072×10^7	-0.03145	13	128	128
1×10^{-6}	0.1	3.245×10^8	-0.01909	23	128	192
5×10^{-4}	1	3.534×10^5	-0.02878	4	64	64
5×10^{-5}	1	6.308×10^6	-0.01812	9	128	128
		Stress-free				
1×10^{-5}	0.1	1.423×10^7	-0.04082	10	64	64

Reasonable initial guesses for Ra_c, m_c and ω_c are possible thanks to previously published results, either from 3-D (Jones *et al.* 2000; Zhang *et al.* 2004, 2007; Zhang & Liao 2017) or columnar flow calculations (Guervilly & Cardin 2016). Furthermore, there exist very well known scaling laws that allow us to estimate Ra_c, m_c and ω_c for a given E from values calculated at higher E, at the same Pr value. These scaling laws are $Ra_c \sim E^{-4/3}$ $m_c \sim E^{-1/3}$, $\omega_c \sim E^{1/3}$ (Roberts 1968; Busse 1970). For each m value close to the estimate m_c (typically $m_c - 10 < m < m_c + 10$ is a wide enough range) we find $Ra_{c,m}$ iteratively via a secant method. At each iteration a new estimate for $Ra_{c,m}$ is found by solving the eigenvalue problem (eqs 37–39) via the Arnoldi method, with shift given by the estimated ω_c, and selecting solutions for which the eigenfrequency is within 10 per cent of this initial estimate. The solution with the largest value of $\mathrm{Re}\{\lambda\}$ is then selected at each iteration. The accuracy goal at which the iterations are stopped is set to $|\mathrm{Re}\{\lambda\}| < 10^{-10}$. Typically the accuracy goal is reached with less than 10 iterations, depending on the initial guess for $Ra_{c,m}$. Once $Ra_{c,m}$ is found for a sufficiently wide range of azimuthal wavenumber m, Ra_c is simply given by the minimal value of $Ra_{c,m}$ and m_c is the corresponding value of m.

Numerical convergence is checked by altering the number of basis set elements N. We consider the result acceptable if $Ra_{c,m}$ is converged to 4 significant digits. Under this criteria, we find that ω_c has converged to a higher number of significant digits and that both the spectra of the solution, $|c_j|$, and m_c do not change with higher resolution.

3.5 Previously published results and complementary 3-D calculations

In this paper, we compare our PG onset calculations against previously published, full-sphere results based on both 3-D (Jones *et al.* 2000; Zhang *et al.* 2004, 2007; Zhang & Liao 2017) and columnar-flow calculations (Guervilly & Cardin 2016). The latter results have been calculated with a state-of-the-art model that makes use of the columnar flow approximation (eq. 9) to describe fluid flows, and the momentum equation is given by the evolution of the vertically averaged, axial vorticity. Another key difference with our PG methodology, is that in Guervilly & Cardin (2016) the temperature evolution is described via the fully 3-D heat eq. (2). This hybrid formulation is the reason we will refer to this model as QG-Hyb. The QG-Hyb model adopts a no-slip boundary layer parametrization akin to the one we adopt (see Section 3.3.1).

Published compilations of onset values in full-sphere geometry have been augmented with full-sphere calculations performed with the `QuICC` numerical code (Marti *et al.* 2016; Marti & Jackson 2021), which is a fully spectral, numerical framework that is capable of solving eqs (1)–(3) in a full sphere. In particular `QuICC` is capable of solving the eigenvalue problems associated with the linearized version of the momentum and temperature equations. The velocity field is described via its poloidal and toroidal potential fields. These scalar quantities, together with temperature, are decomposed as a sum of N_r spherical radial basis functions and L latitudinal functions. The latter are, as is common in the geodynamo community, associated Legendre functions of degree l and order m. The azimuthal wavenumber m being fixed, the maximum order of the expansion is given by the element $l = L$. The critical parameters for the onset of convection are calculated in a similar way as described in the previous section, the most significant difference being that Brent's method is used to maximize $\mathrm{Re}\{\lambda\}$. More details on the numerical methodology implemented in `QuICC` can be found in Marti *et al.* (2016) and Marti & Jackson (2021). Results from the 3-D calculations performed with `QuICC` are summarized in Table 1.

Table 2 provides a reference for the 3-D results (both previously published and derived within the context of this study) results discussed above.

Table 2. Sources of results for the onset of convection in a rotating full sphere. The table indicates, in particular, whether the data consider no-slip or stress-free mechanical boundary conditions. See main text for more information.

Name	Description	Reference
QG-Hyb, no-slip	Columnar/3-D hybrid, no-slip	Guervilly & Cardin (2016)
3-D, no-slip	Fully 3-D, no-slip	Zhang *et al.* (2007); Zhang & Liao (2017); Table 1
3-D, stress-free	Fully 3-D, stress-free	Jones *et al.* (2000); Zhang & Liao (2017)

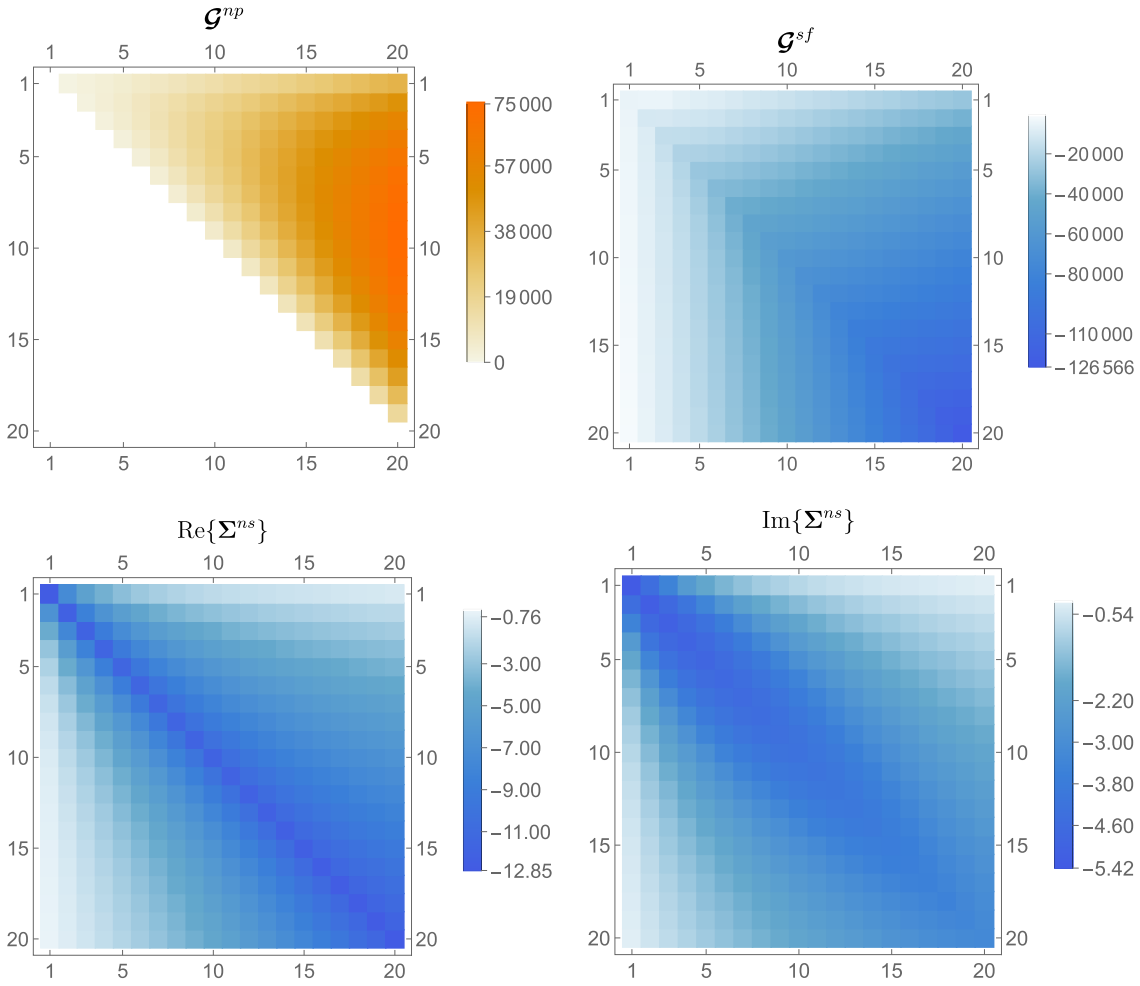

Figure 1. Viscous matrices $\mathcal{G}^{np}$, $\mathcal{G}^{sf}$ and $\boldsymbol{\Sigma}^{ns}$ for $m = 20$ and $N = 20$. The matrices have been calculated, respectively, with formulae (47), (49) and (46), where the basis functions Ψ_j have been normalized so that $\mathcal{N}_{ij} = \delta_{ij}$.

4 RESULTS

4.1 Appraisal of viscous and thermal diffusion

4.1.1 Viscous dissipation

We begin by assessing the validity of the methodology adopted to calculate viscous and thermal diffusion, starting with the parametrized treatment of the viscous boundary layers (see Section 3.3). In Fig. 1, we show the matrix entries for $\mathcal{G}^{np}$, $\mathcal{G}^{sf}$ and $\boldsymbol{\Sigma}^{ns}$.The non-penetration, bulk viscosity matrix $\mathcal{G}^{np}$ has an upper triangular structure, with the diagonal elements being identically zero. This is consistent with previous 3-D (Zhang *et al.* 2001) and columnar-flow (Maffei *et al.* 2017) characterizations of inviscid inertial modes, for which the dissipation integral:

$$\int_{core} (\mathbf{u}_i^m)^* \cdot \nabla^2 \mathbf{u}_j^m \, \mathrm{d}V, \tag{53}$$

is identically zero for $i \geq j$. That this result applies to our PG formalism is remarkable for two reasons. The first is that columnar inertial modes are not a solution to the 3-D problem (Maffei *et al.* 2017) and there is, *a priori*, no reason why the diagonal terms in the dissipation integral should be zero. The second is that the PG equivalent of eq. (53) has been derived in a different way. Specifically, eq. (53) explicitly

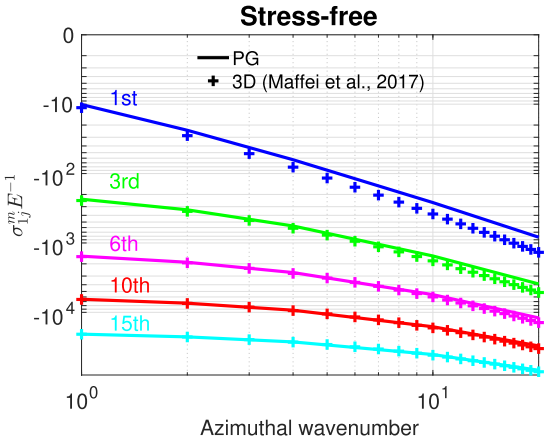

Figure 2. First order, stress-free viscous corrections to the inertial modes eigenfrequency. The PG corrections (full lines) have been calculated as in eq. (55) but are rescaled by E^{-1}. The 3-D corrections (crosses) are as reported in Maffei *et al.* (2017) and are computed for the 3-D, QGIW modes as in Liao *et al.* (2001). The horizontal axis shows the azimuthal wavenumber m and the radial order of the solution is shown in the plots, with the dark-blue line indicating the viscous corrections to the fundamental inviscid modes.

involves a projection of $\nabla^2\mathbf{u}_j^m$ on the velocity $\mathbf{u}_i^m$, while eq. (47) involves a projection of the viscous operator $(F_V)_j^m$ on the stream-function Ψ_i^m. It is far from obvious that the two formulations should be equivalent for $i < j$, and future work will explore this property. A proof of the vanishing of the diagonal terms of eq. (53) for columnar flows is given in Appendix D. The fact that the non-zero entries of $\mathcal{G}_{ij}^{np}$ are all positive is consistent with other columnar-flow formulations (Maffei *et al.* 2017) and in contrast with 3-D calculations, for which the dissipation integral is either positive or negative for $i < j$. The real parts of the stress-free, $\boldsymbol{\mathcal{G}}^{sf}$, and no-slip, $\boldsymbol{\Sigma}^{ns}$ integrals are non-zero and negative along the diagonal, indicating, as expected, a decay of the corresponding inertial mode. Also note that, while $\boldsymbol{\mathcal{G}}^{sf}$ is fully real-valued, the entries of $\boldsymbol{\Sigma}^{ns}$ are generally complex.

To estimate the effect of no-slip and stress-free parametrizations, we computed the first-order viscous corrections with respect to the inviscid solution, following the procedure outlined in Maffei *et al.* (2017). These corrections are an estimate valid for low-E values and are entirely calculated from the inviscid solution. The viscous inertial mode problem is obtained by reinstating viscosity in eq. (40) or, equivalently, setting $Ra = 0$ in eq. (24). The first-order perturbative solution is given by (Liao *et al.* 2001; Liao & Zhang 2008; Maffei *et al.* 2017):

$$\mathbf{u} = \sum_{j=1}^{N} c_j \left(\mathbf{u}_j^m + (\mathbf{u}_1)_j^m\right) \mathrm{e}^{\mathrm{i}m\phi + (\mathrm{i}\omega_j^m + \mathrm{i}\omega_{1j}^m + \sigma_{1j}^m)t}, \tag{54}$$

where $\mathbf{u}_j^m$, ω_j^m are given by the inviscid solutions (eqs 31 and 36) and $(\mathbf{u}_1)_j^m$, ω_{1j}^m, σ_{1j}^m are first order, small viscous perturbations. Here we assume that ω_{1j}^m and σ_{1j}^m are purely real, so that they unequivocally refer to, respectively, the frequency correction and the damping factor. Introducing eq. (54) in eq. (24) with $Ra = 0$, implementing viscous boundary conditions as detailed in Section 3.3 and following a procedure analogous to Maffei & Jackson (2016), it is found that:

$$\mathrm{i}\omega_{1j}^m + \sigma_{1j}^m = E\frac{\mathcal{G}_{jj}^{sf}}{\mathcal{N}_{jj}}, \tag{55}$$

$$\mathrm{i}\omega_{1j}^m + \sigma_{1j}^m = E^{1/2}\frac{\Sigma_{jj}^{ns}}{\mathcal{N}_{jj}}, \tag{56}$$

in, respectively, the stress-free and no-slip cases. In the above formulae the notation $\mathcal{G}_{jj}^{sf}$ refers to the diagonal jth term of the matrix $\boldsymbol{\mathcal{G}}^{sf}$ and not to its trace. We did not make use of the assumption that $\mathcal{N}_{ij} = \delta_{ij}$ for generality, as the viscous corrections are independent of this particular choice. In Fig. 2 and 3 we compare first-order, viscous corrections for the PG model, obtained via eqs (55) and (56), and for the 3-D, QGIW solutions first derived in Zhang *et al.* (2001). For the latter, viscous corrections are calculated via a methodology similar to the one that led to eqs (55) and (56), and outlined in Liao *et al.* (2001). The values for the 3-D corrections shown in Figs 2 and 3 by the crosses, are the same as published in Maffei *et al.* (2017).

For stress-free, the calculation eq. (55) predicts a purely real correction to the inviscid eigenfrequencies ω_j^m indicating that, at first order, stress-free boundaries introduce a viscous decay to the inviscid solution, but no modifications on the frequencies (i.e. $\omega_{1j}^m = 0$). This is a consequence of the purely real nature of the entries of $\boldsymbol{\mathcal{G}}^{sf}$ and is in agreement with the 3-D correction. For no-slip, both ω_{1j}^m and σ_{1j}^m are non-zero, in line with 3-D calculations. The agreement with the 3-D correction is quantitatively better for the decay rate σ_{1j}^m than for the frequency correction ω_{1j}^m, but is worse than for the stress-free case. We attribute the no-slip mismatch to the zero-frequency approximation used to derive eq. (42), since the 3-D, no-slip corrections have been derived in the general case where the boundary layer correction depends on the frequency ω_j^m of the inviscid mode considered. Note that both the PG inviscid eigenfrequencies (see fig. 1 in Paper 1) and the stress-free, first-order corrections agree well with 3-D calculations. Therefore we speculate that the origin of the disagreement with 3-D,

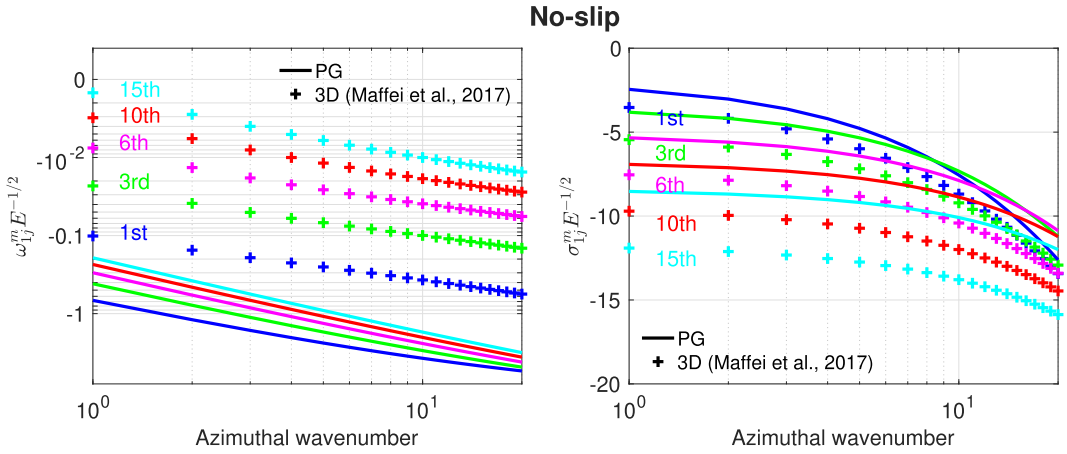

Figure 3. First order, no-slip viscous corrections to the inertial modes eigenfrequency. The PG corrections (full lines) have been calculated as in eq. (56) but are rescaled by $E^{-1/2}$. The 3-D corrections (crosses) are as reported in Maffei *et al.* (2017) and are computed for the 3-D, QGIW modes as in Liao *et al.* (2001). The horizontal axis shows the azimuthal wavenumber m and the radial order of the solution is shown in the plot.

no-slip calculations, is not unique to our PG model, but it is shared among all other columnar-flow models that make use of eq. (42) to describe the Ekman pumping flow. Further analysis will be carried on in future studies.

4.1.2 *Thermal diffusion*

Next we turn our attention to the assessment of the approximation involved in the derivation of the thermal diffusion terms (eqs 22 and 23). With `QuICC` we obtained the temperature at the onset of thermal convection for various combinations of the Pr and E numbers (see Table 1). The diffusive term $\nabla^2 T$ was then calculated in physical space using the finite difference `Python` package `findiff` (Baer 2018). We focussed on the meridional contribution:

$$\nabla_m^2 T = \frac{1}{r^2}\frac{\partial}{\partial r}\left(r^2\frac{\partial T}{\partial r}\right) + \frac{1}{r^2\sin\vartheta}\frac{\partial}{\partial\theta}\left(\sin\theta\frac{\partial T}{\partial\theta}\right),$$

since the azimuthal contributions (proportional to the second derivatives in ϕ) only involves differential operators that commute with the vertical integration operators. The validity of the approximations (22) and (23) is therefore not affected by the azimuthal contributions. In the left-hand panels of Fig. 4 we show $\nabla_m^2 T$ for the solution at the onset of convection for $E = 5\times10^{-4}$ and $E = 5\times10^{-5}$, both calculated for $Pr = 0.1$. As can be seen, the quantity $\nabla_m^2 T$ exhibits the expected spatial anisotropy, with a tendency for invariance along the z direction. This tendency increases as E decreases.

We then assessed the validity of the approximations (21), (22) and (23) by calculating $\langle\nabla_m^2 T\rangle$, $\overline{\nabla_m^2 T}$, $\widetilde{z\nabla_m^2 T}$ and corresponding PG approximations, from the 3-D solution. Note that the meridional component of the equatorial Laplacian ∇_e^2 only involves derivatives in s. That is:

$$\nabla_m^2\overline{T} = \frac{1}{s}\frac{\partial}{\partial s}\left(s\frac{\partial\overline{T}}{\partial s}\right),$$

and similarly for $\langle T\rangle$ and $\widetilde{zT}$. Vertical integrals where calculated by interpolating the 3-D solution on a rectangular grid in s and z and using the `scipy` function `romb` to perform vertical integrals via the Romberg method. We experimented with various integration methods and rectangular grid spacing in order to obtain visually smooth results. The numerical accuracy of our methodology has not been thoroughly tested, but the correctness of our method has been visually checked by applying it to functions of s and z for which calculations of the quantities of interests was possible analytically (not shown).

From the results in Fig. 4 we conclude that the approximations (21), (22) and (23) are indeed valid, and that their validity increases with increasing complexity of the underlying 3-D solution in the equatorial direction, which is expected, for fixed Pr at low-E values. In the same Figure, we also illustrate, in blue, the failure of the more simple approximations $\overline{\nabla^2 T} \simeq \nabla^2\overline{T}$ and $\widetilde{z\nabla^2 T} \simeq \nabla^2\widetilde{zT}$, which intuitively lead to simpler mathematical and numerical treatment. Although these alternative prescriptions lead to better approximations in the interior of the domain, they fail as the boundary $s = 1$ is approached. In particular, $\nabla^2\overline{T}$ becomes singular. The mathematical reason for that can be understood by expanding the radial dependence of $\overline{T}$ and $\widetilde{zT}$ as a sum of the basis elements defined in eqs (32) and (33). Note that these expansions are consistent with the discretization approaches used in 3-D numerical codes, such as `QuICC`. The presence of the H^3 and H^4 pre-factors in eqs (32) and (33), introduced to reflect the vertical integral operations (eqs 12 and 13) and the fixed-temperature boundary conditions (eq. 5), causes $\nabla^2\overline{T}$ and $\nabla^2\widetilde{zT}$ to be, respectively, singular and non-zero in $s = 1$, in opposition to the behaviour of the desired diffusion terms $\overline{\nabla^2 T}$ and $\widetilde{z\nabla^2 T}$. The H^{-1} and H^{-2} factors in eqs (22) and (23) remove a similar pre-factor in eqs (32) and (33), introduced to reflect the application of eqs (12) and (13) to the original temperature field. In particular, the quantity $\overline{T}H^{-1}$ is now a polynomial in s^2 and

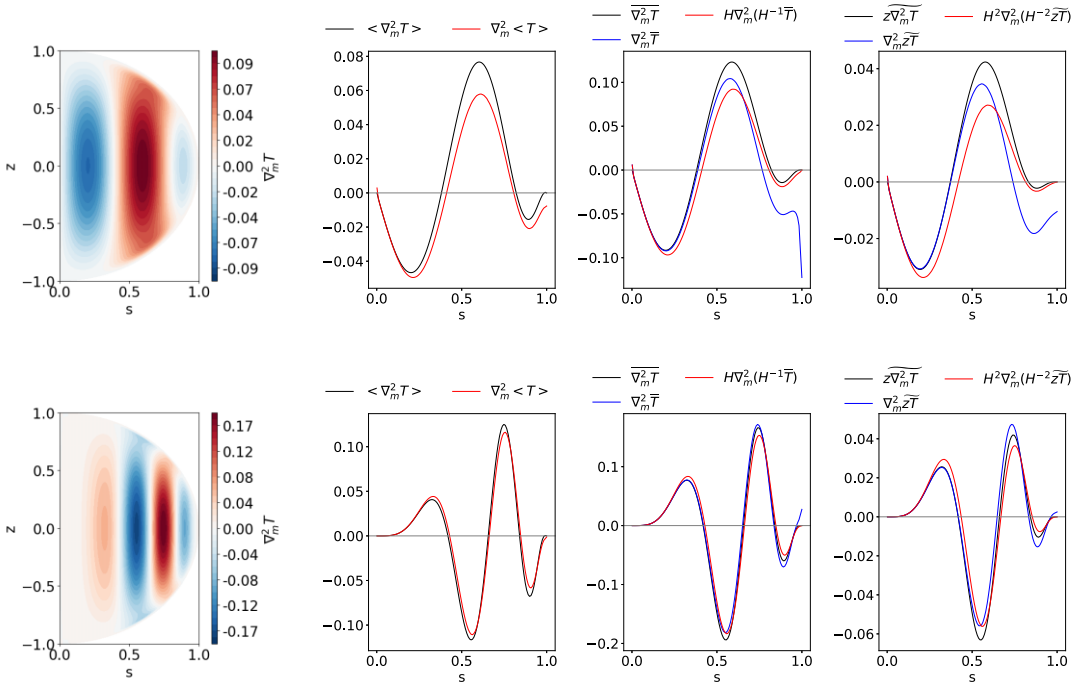

Figure 4. Comparison between the approximated, PG thermal diffusive term and the non-approximated version from 3-D calculations. The top and bottom rows refers to the onset of convection calculated for $Pr = 0.1$ and, respectively, $E = 5 \times 10^{-4}$ and $E = 5 \times 10^{-5}$. Only the meridional (along r and θ in the 3-D case, s in the vertically averaged case) contributions to the diffusive terms are considered. The density plots on the left illustrate the meridional diffusive contribution as derived from 3-D results.

its derivatives are not problematic anymore. The multiplication by H and H^2 after the application of ∇_e^2 restores the desired parity and the correct behaviour in $s = 1$.

We remark that the diffusion forms eqs (22) and (23) have been derived empirically and their physical and mathematically consistency has not been fully checked. Future work will involve testing these forms against well-established criteria, such as whether they lead to unphysical dissipation (Shchepetkin & O'Brien 1996).

4.2 Asymptotic onset of thermal convection

The calculation of critical onset values for asymptotically low E and spherical geometries is a classical problem tackled by multiple landmark studies (Chandrasekhar 1961; Roberts 1968; Busse 1970; Jones *et al.* 2000). In particular, the Roberts–Busse annulus theory (Roberts 1968; Busse 1970) is a well-known staple of rapidly rotating thermal convection. In this Section we show that a similar asymptotic analysis, performed on the PG set of linear eqs (24)–(26), provides an updated and upgraded low-E solution.

We follow the classical Roberts–Busse, local theory and look for a solution for which the azimuthal scales are much smaller than the radial ones. We therefore assume that:

$$\left|\frac{\partial \Psi}{\partial s}\right| \ll \left|\frac{1}{s}\frac{\partial \Psi}{\partial \phi}\right|, \tag{57}$$

and similarly for $\overline{T}$ and $\widetilde{zT}$. Furthermore we assume oscillatory solutions in t and ϕ and make the substitutions:

$$\frac{\partial \Psi}{\partial \phi} = \mathrm{i}m\Psi \tag{58}$$

$$\frac{\partial \Psi}{\partial t} = \mathrm{i}\omega\Psi \tag{59}$$

where the last assumption derives from requiring that the growth rate of the solution is zero. In line with the simplified local derivation detailed in section 8.05.4.5.1 of Jones (2015), we only apply non-penetration boundary conditions, and neglect the effect of stress-free or no-slip boundaries on the tangential velocity components. Including these effects would considerably complicate the following derivation, which is solely aimed at obtaining a leading order behaviour for low-E values. We insert assumptions (57)–(59) in the linear system (24)–(26) and, in each term of the equations, only retain the dominant terms arising from the spatial derivatives, according to eq. (57). This leads to:

$$\frac{m^2}{H}\left(-\frac{s}{2H^2}-\frac{1}{s}\right)\mathrm{i}\omega\Psi = \frac{2s}{H^3}\mathrm{i}m\Psi + E\frac{m^4}{2s^3H^3}(2-s^2)\Psi + \frac{1}{2H}RaE^2\mathrm{i}m\left(s\overline{T}-\frac{s}{H}\widetilde{zT}\right), \tag{60}$$

$$\left(\mathrm{i}\omega + \frac{E}{Pr}\frac{m^2}{s^2}\overline{T}\right) = \frac{1}{Pr}\frac{4}{3}\mathrm{i}ms\Psi, \tag{61}$$

$$\left(\mathrm{i}\omega + \frac{E}{Pr}\frac{m^2}{s^2}\widetilde{zT}\right) = \frac{1}{Pr}\frac{1}{2}\mathrm{i}ms\Psi. \tag{62}$$

Note that the last two equations are insensitive to the use of approximations (22) and (23), since they only involve azimuthal derivatives, assumed to be dominant with respect to the radial ones.

Eqs (60)–(62) can be combined into a single equation for Ψ, from which the following characteristic equation can be obtained:

$$\left(\mathrm{i}\omega + \frac{E}{Pr}\frac{m^2}{s^2}\right)\left[\frac{m^2}{H}\left(-\frac{s}{2H^2} - \frac{1}{s}\right)\mathrm{i}\omega - \frac{2s}{H^3}\mathrm{i}m - E\frac{m^4}{2s^3H^3}(2-s^2)\right] + RaE^2m^2\frac{5}{6}\frac{s}{H} = 0.$$

By separately solving the imaginary and real part of the above equation we obtain:

$$\omega = \frac{4s^2}{m(Pr+1)(s^2-2)}, \tag{63}$$

$$Ra = \frac{6\left(16Pr^2s^8 + E^2m^6(Pr+1)^2\left(s^2-2\right)^2\right)}{5E^2m^2(Pr+1)^2s^6\left(s^4-3s^2+2\right)}. \tag{64}$$

By minimising these expressions for Ra and ω with respect to s and m we obtain the critical values:

$$s_c = \sqrt{1-\sqrt{\frac{3}{5}}} = 0.474767 \tag{65}$$

$$m_c = \frac{2^{2/3}}{\left(5(244+63\sqrt{15})\right)^{1/6}}\left(\frac{Pr}{E(1+Pr)}\right)^{1/3} = 0.432635\left(\frac{Pr}{E(1+Pr)}\right)^{1/3} \tag{66}$$

which, substituted back in eqs (63) and (64) leads to

$$Ra_c = 12\frac{2^{2/3}\sqrt{3}}{5^{1/6}\left(\frac{Pr}{E(1+Pr)}\right)^{4/3}} = 25.2309\left(\frac{Pr}{E(1+Pr)}\right)^{4/3} \tag{67}$$

$$\omega_c = -\frac{2^{4/3}5^{1/6}}{\sqrt{4+\sqrt{15}}}\left(\frac{E}{Pr}\right)^{1/3}\frac{1}{(1+Pr)^{2/3}} = -1.7435\left(\frac{E}{Pr}\right)^{1/3}\frac{1}{(1+Pr)^{2/3}}. \tag{68}$$

The above estimate should be compared with the classical Roberts–Busse local theory (indicated via the RB subscript):

$$s_{c,RB} = \frac{1}{\sqrt{5}} = 0.447214 \tag{69}$$

$$m_{c,RB} = \frac{5^{1/6}}{\sqrt{2}}\left(\frac{Pr}{E(1+Pr)}\right)^{1/3} = 0.924656\left(\frac{Pr}{E(1+Pr)}\right)^{1/3}, \tag{70}$$

$$Ra_{c,RB} = 5^{2/3}\frac{15}{4}\left(\frac{Pr}{E(1+Pr)}\right)^{4/3} = 10.9651\left(\frac{Pr}{E(1+Pr)}\right)^{4/3} \tag{71}$$

$$\omega_{c,RB} = \frac{5^{1/3}}{\sqrt{2}}\left(\frac{E}{Pr}\right)^{1/3}\frac{1}{(1+Pr)^{2/3}} = -1.20914\left(\frac{E}{Pr}\right)^{1/3}\frac{1}{(1+Pr)^{2/3}}. \tag{72}$$

Comparing the two, we see that both the PG and the Roberts–Busse asymptotic theories capture the same behaviour with E and Pr. The numerical pre-factors are different, with our PG, asymptotic theory predicting a larger Rayleigh number, Ra_c, and drift rate, ω_c, and a smaller azimuthal wavenumber, m_c. The predicted radial location at which convective perturbations grow first, s_c, is slightly larger in our theory. Note that both Roberts–Busse theory and our own assume columnar flows, though the former makes use of a simpler version of eq. (9).

Representative asymptotic and 3-D solutions for two different combinations of E and Pr are reported in Table 3. These values have been obtained in a regime [referred to as the 'viscous convection' by Zhang & Liao (2017)] in which the 3-D solution can be meaningfully compared with the asymptotic calculations above. In this regime, viscosity enters the leading order force balance and the onset of thermal convection takes the form highly columnar structures travelling in the prograde direction. In this regime, Table 3 shows that our asymptotic PG theory is in better agreement with 3-D numerical results when compared to the classical Roberts–Busse theory. We also note that both the PG and Roberts–Busse asymptotic theories perform significantly better for $Pr = 1$ than for more characteristic values for Earth's core conditions, such as $Pr = 0.1$. This is a known limitation of asymptotic theories derived as above (Zhang 1992; Guervilly & Cardin 2016) and it is due to the restrictiveness of the starting assumption (eq. 57). A more general asymptotic solution has been derived in Jones *et al.* (2000) by using a global theory that captures the correct spatio-temporal behaviour of the solution. In particular the correct asymptotic behaviour $\sim E^{1/3}$ is preserved in both the azimuthal and radial direction. The Pr number dependency, however, is not explicitly given but has been computed numerically for $0.01 \leq Pr \leq 100$ in Jones *et al.* (2000).

Table 3. Low-E, asymptotic calculations compared with 3-D calculations for the two cases indicated in the Table: $Pr = 1$; $E = 1 \times 10^{-4}$ (top) and $Pr = 0.1$; $E = 1 \times 10^{-5}$ (bottom). 3-D solution have either been taken from known references or from novel calculations (see Table 2). The PG, asymptotic solution, calculated via formulae (66)–(68), is highlighted for both cases. The rows indicated with 'Roberts–Busse theory' reports values calculated via formulae (70)–(72), which have been adapted from Busse (1970). The rows indicated with 'Jones–Soward–Mussa theory' reports values calculated via the leading order expansion derived in Jones *et al.* (2000) (see 'Absolute instability results' in their table 2).

Calculation	Ra_c	ω_c	m_c
$Pr = 1$; $E = 1 \times 10^{-4}$			
3-D, stress-free	2.64×10^6	−0.0326	8
3-D, no-slip	2.58×10^6	−0.0228	7
PG, asymptotic	$\mathbf{2.16 \times 10^6}$	**−0.0343**	**7.4**
Roberts–Busse theory	0.938×10^6	−0.0354	15.8
Jones–Soward–Mussa theory	2.24×10^6	−0.0347	8.2
$Pr = 0.1$; $E = 1 \times 10^{-5}$			
3-D, stress-free	1.42×10^7	−0.0408	10
3-D, no-slip	1.67×10^7	−0.0403	11
PG, asymptotic	$\mathbf{4.79 \times 10^6}$	**−0.0512**	**9.0**
Roberts–Busse theory	2.08×10^6	−0.0527	19.3
Jones–Soward–Mussa theory	1.32×10^7	−0.0424	10.4

Table 4. Onset of thermal convection results computed with the PG model, with no-slip boundary conditions. In the Table we report the E and Pr combinations for the calculations, the resulting critical parameters Ra_c, ω_c and m_c, the radial resolution N and the index of the dominant radial mode j_{max}. The latter is defined via the maximum value of the stream-function spectra $|c_j|$. The reported value of N is not an accurate estimation of the minimal resolution required for convergence, but it is indicated here for transparency.

E	Pr	Ra_c	ω_c	m_c	N	j_{max}
1×10^{-4}	0.1	1.110×10^6	−0.07849	4	40	2
1×10^{-5}	0.1	2.005×10^7	−0.04119	10	50	5
1×10^{-6}	0.1	3.888×10^8	−0.01972	22	80	12
1×10^{-7}	0.1	7.968×10^9	−0.009667	53	80	26
1×10^{-8}	0.1	1.656×10^{11}	−0.004319	102	100	57
1×10^{-3}	1	1.883×10^5	−0.04134	2	20	1
1×10^{-4}	1	3.208×10^6	−0.02943	7	20	3
1×10^{-5}	1	6.197×10^7	−0.01522	16	20	7
1×10^{-6}	1	1.267×10^9	−0.007450	35	60	17
1×10^{-7}	1	2.659×10^{10}	−0.003570	76	70	36

4.3 Onset of thermal convection calculations

Numerical results for the critical parameters Ra_c, m_c and ω_c in the general case (i.e. retaining all spatial derivatives) were obtained for various values of Pr and E by solving the PG linear system (24)–(26) via the methodology outlined in Section 3. We focussed on Pr values of 0.1 and 1 due to their significance in the study of thermal convection in Earth's outer core, and the availability of existing results in the literature (see Table 2 and Section 3.5). PG calculations were performed under both no-slip and stress-free boundary conditions, using the boundary layer parametrizations introduced in Sections 3.3.1 and 3.3.2, respectively.

Results from our calculations are shown in Tables 4 and 5, and Figs 5 and 6.

Fig. 5 shows values of Ra_c, m_c and ω_c, as a function of E for both $Pr = 0.1$ and $Pr = 1$. The scaling derived from our no-slip calculations for $E \leq 10^{-5}$ are also reported in Fig. 5. Note that our scalings are close to the expected ones for both $Pr = 0.1$ and $Pr = 1$. Fig. 6 reports the same data as Fig. 5, but compensated for the expected scaling behaviour for low E illustrated in relationships (66)–(68).

Analysing Figs 5 and 6 reveals that the PG model's results are in line with 3-D calculations and expected scaling behaviours at low-E. In particular we see that for stress-free, the critical Rayleigh number Ra_c is lower than for no-slip (see Figs 5 and 6). The expected asymptotic behaviour $Ra_c \sim E^{-4/3}$ is reached for higher values of E under stress-free conditions, at least for the $Pr = 0.1$ case (see Fig. 6). The same behaviour is hinted at in our $Pr = 1$ results, but lower E calculations are needed to confirm this observation. The compensated evolution for m_c and ω_c, appears less monotonic than for Ra_c, both for 3-D and PG calculations, especially for $Pr = 0.1$. For $Pr = 1$, both m_c and ω_c seem to approach the expected asymptotic regimes at low E. As E becomes smaller, differences in the results from the no-slip and stress-free implementations tend to reduce. This is especially clear from the compensated Ra_c behaviour and is as expected since boundary layer effects on the solution can be considered as perturbations that vanish for $E \to 0$ (Zhang & Jones 1993).

Table 5. Onset of thermal convection results computed with the PG model, with stress-free boundary conditions. See caption of Table 4 for details on the entries.

E	Pr	Ra_c	ω_c	m_c	N	j_{max}
6.324×10^{-5}	0.1	1.483×10^{6}	-0.06266	4	20	3
2×10^{-5}	0.1	6.630×10^{6}	-0.04957	7	20	4
1×10^{-5}	0.1	1.673×10^{7}	-0.03992	9	20	6
6.324×10^{-6}	0.1	3.123×10^{7}	-0.03316	10	30	7
3.660×10^{-6}	0.1	6.400×10^{7}	-0.02823	12	50	8
1×10^{-6}	0.1	3.599×10^{8}	-0.02062	24	50	12
1×10^{-7}	0.1	7.714×10^{9}	-0.01005	57	60	26
1×10^{-8}	0.1	1.610×10^{11}	-0.004349	102	100	58
6.324×10^{-5}	1	5.452×10^{6}	-0.03286	9	10	4
2×10^{-5}	1	2.418×10^{7}	-0.02164	13	30	6
1×10^{-5}	1	5.976×10^{7}	-0.01711	16	30	8
6.324×10^{-6}	1	1.089×10^{8}	-0.01482	19	50	9
2×10^{-6}	1	4.952×10^{8}	-0.01028	29	80	14
1×10^{-6}	1	1.236×10^{9}	-0.008133	36	30	17
1×10^{-7}	1	2.614×10^{10}	-0.003778	77	80	38

Comparison with results from the QG-Hyb shows that our PG methodology has superior performance, since our no-slip results are generally closer to the 3-D predictions, with the notable exception of ω_c for the $Pr = 1$ cases. Furthermore, analysis of the compensated Ra_c data for $Pr = 0.1$, show that the PG model approaches the expected $Ra_c \sim E^{-4/3}$ law, for both no-slip and stress-free implementations. Conversely, the QG-Hyb results do not show sign of convergence even at $E = 10^{-8}$.

In Figs 7 and 8, we show the solution in physical space for Ψ, $\overline{T}$ and $\widetilde{zT}$, for the no-slip onset modes at $Pr = 0.1$ and, respectively $E = 10^{-4}$ and $E = 10^{-6}$. In these Figures we only show a quarter of the equatorial disc, in order to highlight details of the solutions that would be difficult to see if the full domain were to be shown. All solutions are periodic in ϕ. Figs 7 and 8 illustrate many of the typical characteristics of the onset of thermal convection in spherical domains: the spiralling nature of both velocity and temperature solutions, and that as E decreases, the spatial complexity increases, in agreement with the scaling $m_c \sim E^{-1/3}$ derived via asymptotic calculations.

Our results show that the radial complexity of the onset solution scales in a similar fashion, which is at the origin of the spiralling nature of the solution. We show this in Fig. 9 were we plot the index, j_{max} at which the spectra, $|c_j|$, of the stream-function solution, reaches its maximum value. In Fig. 9, we compensate j_{max} for the $E^{-1/3}$. The figure indicates that both m_c and j_{max} have a similar scaling behaviour. This shows the inadequacy of the asymptotic assumption (57), essentially requiring that $m_c/j_{max} \sim E^{-1/3}$.

The novel aspect of these PG solutions is the existence of two temperature variables, $\overline{T}$ and $\widetilde{zT}$. As is seen in Figs 7 and 8, the two are visually very similar to each other. This is expected since the 3-D solutions in these regime show that the temperature field has a high degree of axial invariance. Therefore $\overline{T}$ and $\widetilde{zT}$, being two different vertically integrated moments of the same variable, show basically the same equatorial structure. The main difference is their amplitude, with $\widetilde{zT} < \overline{T}$, which is consistent with their definitions and from the fact that $|z| < 1$.

5 CONCLUSIONS

In summary, we derived a novel columnar-flow model to study thermal convection in Earth's outer core. This formulation is based on the PG equations presented in Paper 1, which have been extended by the inclusion thermal effects and of viscous mechanical boundary conditions, and does not require the assumptions on the geometry of the original temperature field.

The inclusion of viscous corrections allow a parametrization of the effect of either no-slip or stress-free, mechanical boundary conditions. This has been achieved by adapting existing solutions to the PG formulation. For the no-slip case, a well known parametrization of the Ekman pumping term (Schaeffer 2004; Schaeffer & Cardin 2005a, b), results in an additional term, introduced in the momentum equation, proportional to $E^{1/2}$. A well known issue of this approach is the singularity of this term at the equatorial boundary, $s = 1$. For stress-free conditions, a methodology first introduced in Zhang (1994) and adapted to columnar-flow models in Maffei *et al.* (2017), has been extended to the PG formalism. The viscous correction introduced in this case is proportional to E. First order calculations revealed that the resulting viscous corrections are in satisfactory agreement with 3-D results, particularly for the stress-free case (see Figs 2 and 3).

The derivation of the Ekman pumping eq. (42) warrants some additional considerations. First, without assuming low-frequency motions, a general form of $u_{1r}|_{\pm H}$ can be derived assuming that the interior flow is a superposition of inertial waves (Kudlick 1966). In this case the singular pre-factor $1/\sqrt{H}$ is replaced by terms proportional to $1/\sqrt{\mathrm{i}(\omega_j^m \pm 2H)}$, where ω_j^m is the frequency of a given inertial mode. The form $u_{1r}|_{\pm H}$ is therefore singular at the critical latitudes, defined by the condition $\omega_j^m \pm 2\cos\theta = 0$. This singularity, located in the interior of the domain, $s < 1$, is still integrable for columnar modes (Maffei *et al.* 2017). A numerically efficient methodology, akin to Gaussian quadrature, is however not readily available. In current columnar-flow models this general pumping form is not implemented because the inertial mode frequencies appear explicitly in the formulation. Unless the flow is expressed as a superposition of inertial modes, this presents considerable

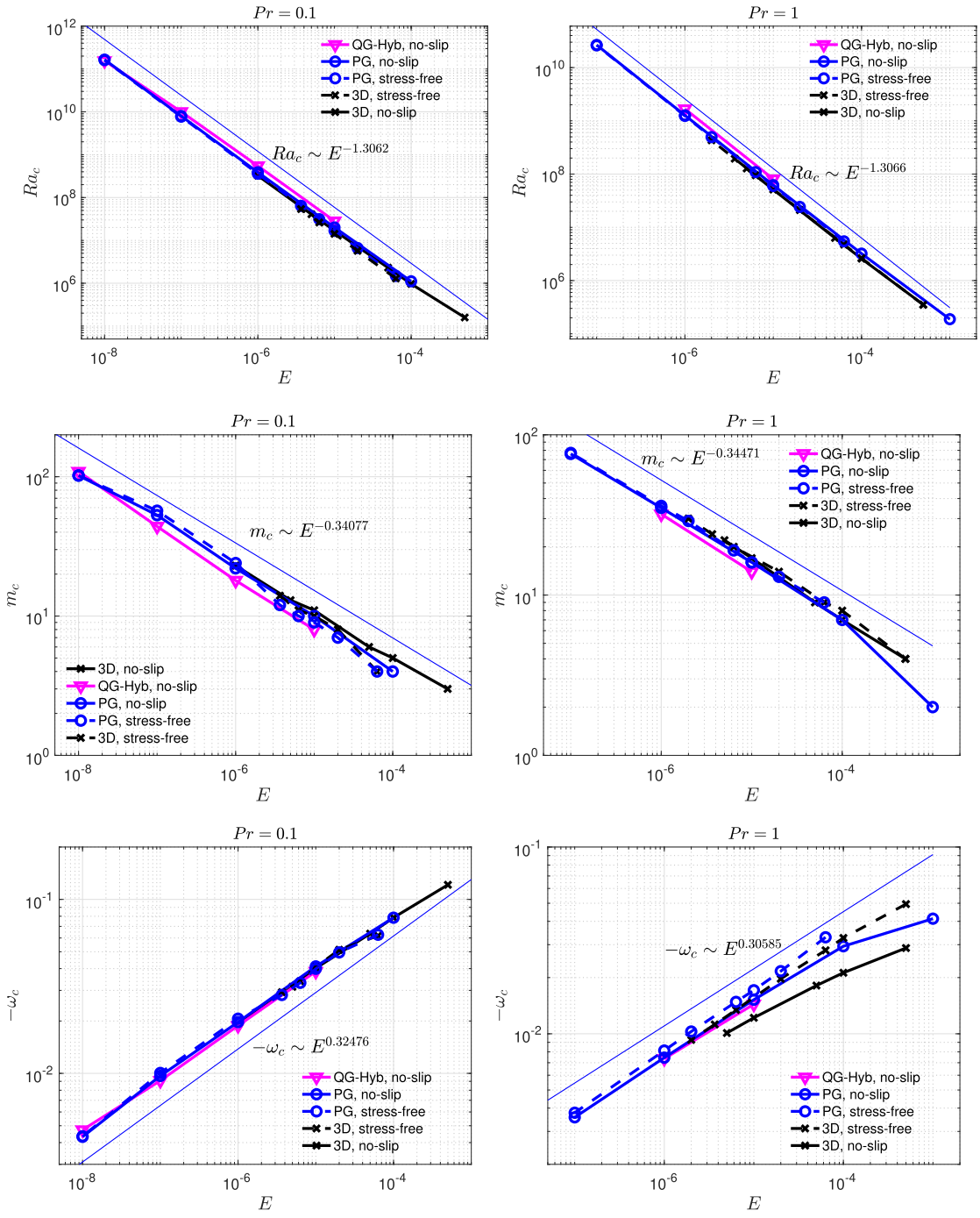

Figure 5. Onset of thermal convection calculations. The above plots illustrate the critical values Ra_c, m_c and ω_c (resp. top, middle and bottom rows) for $Pr = 0.1$ (left-hand side) and $Pr = 1$ (right-hand side). The blue lines show results from our PG calculations, the magenta lines are results from the QG model of Guervilly & Cardin (2016); Guervilly *et al.* (2019), the black lines are unapproximated, 3-D calculations from Jones *et al.* (2000), Zhang *et al.* (2007) and Zhang & Liao (2017), complemented with the results from Table 1 (see Table 2). Full and dashed lines refer, respectively, to no-slip and stress-free calculations. The thin blue line illustrates the slope of the scaling behaviour with E calculated from no-slip, PG calculations for $E \leq 10^{-5}$.

issues. Our PG formulation makes use of such a decomposition (see eq. 31) and it will be possible, in future studies, to explore the effect of a more general form of eq. (42).

Another caveat to formula (eq. 42) is that it represents a first order viscous correction. A more comprehensive treatment of the boundary layer (Kida 2011) reveals that the singularity is removed by embedding the critical latitudes in a region of thickness $\sim E^{-2/5}$ and lateral width $\sim E^{-1/5}$, in agreement with theoretical predictions (Roberts & Stewartson 1963). This correction has not been considered here primarily because of its cumbersome numerical implementation (Kida 2011).

The buoyancy term in the PG momentum eq. (10) is fully described by the two, 2-D thermal quantities $\overline{T}$ and $\widetilde{zT}$. In agreement with the columnar-flow approximation (eq. 9) and the linear nature of the buoyancy term (eq. 17), these quantities are two different moments of the

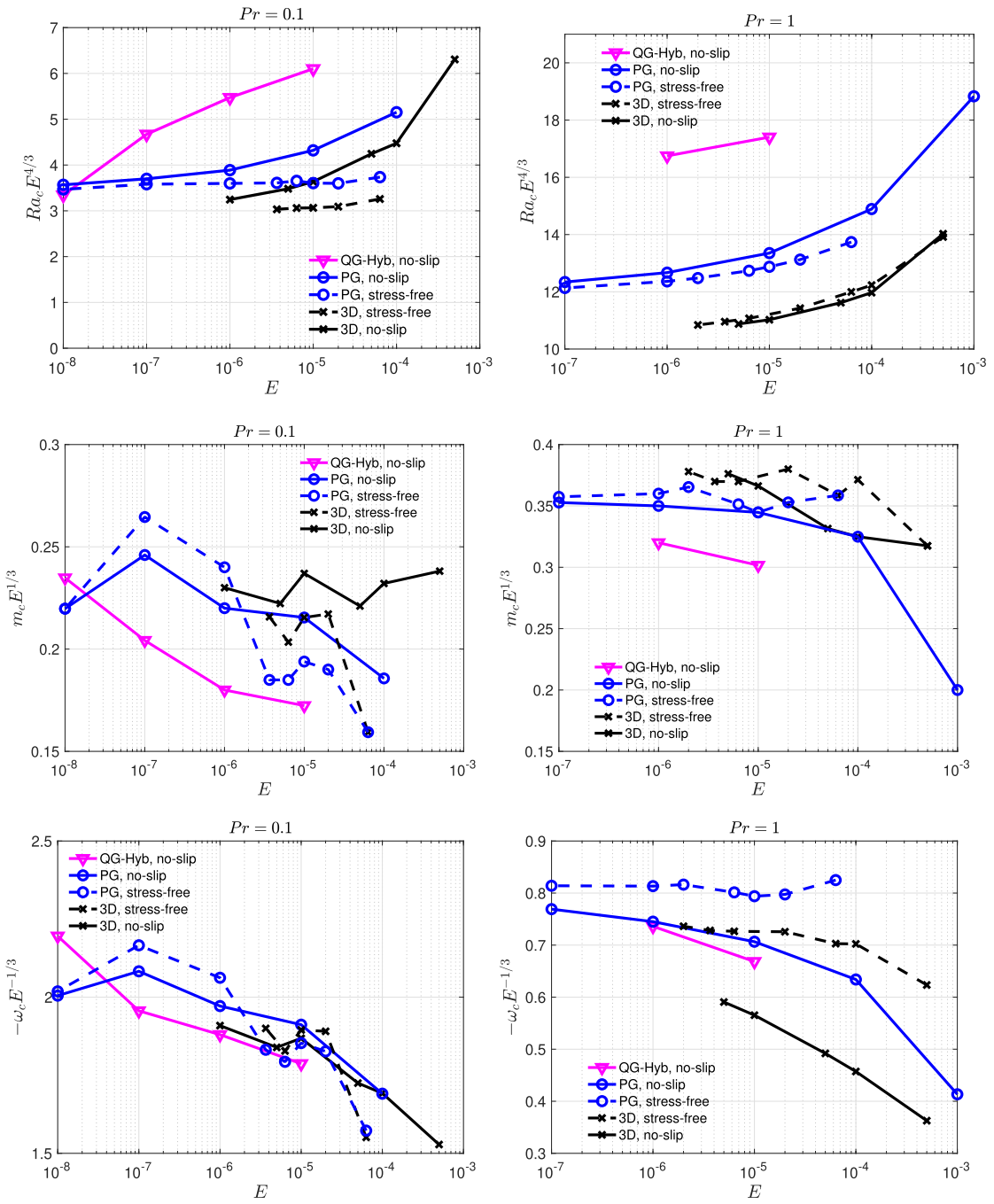

Figure 6. Same as Fig. 5, but results are corrected by the expected scaling behaviours (namely, $Ra_c \sim E^{-4/3}$, $m_c \sim E^{-1/3}$, $\omega_c \sim E^{1/3}$). Flat lines towards the left of the plots indicate that results have reached expected asymptotic behaviours.

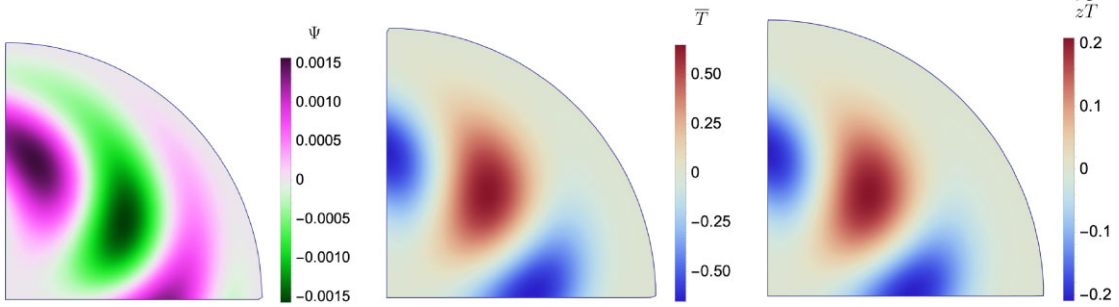

Figure 7. Equatorial plots of (from left to right) Ψ, $\overline{T}$ and $\widetilde{zT}$ at the onset of convection for $Pr = 0.1$, $E = 10^{-4}$ in the no-slip case. Only a quarter of the equatorial circle is shown. For this case: $m_c = 4$.

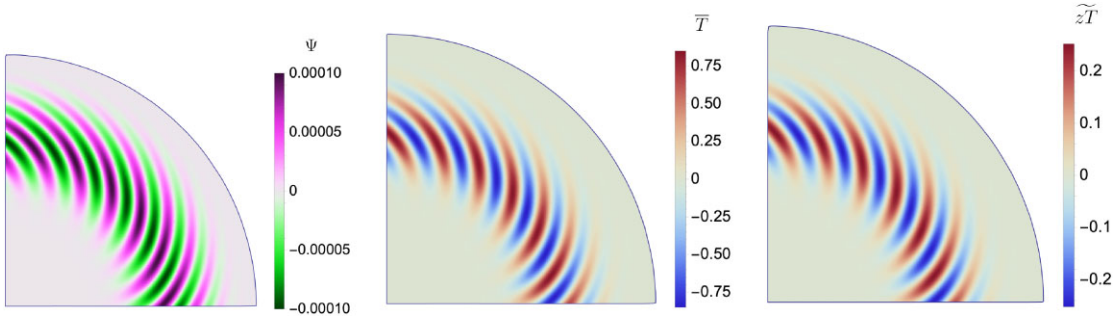

Figure 8. Same as Fig. 7 but for the case $E = 10^{-6}$. For this case $m_c = 23$.

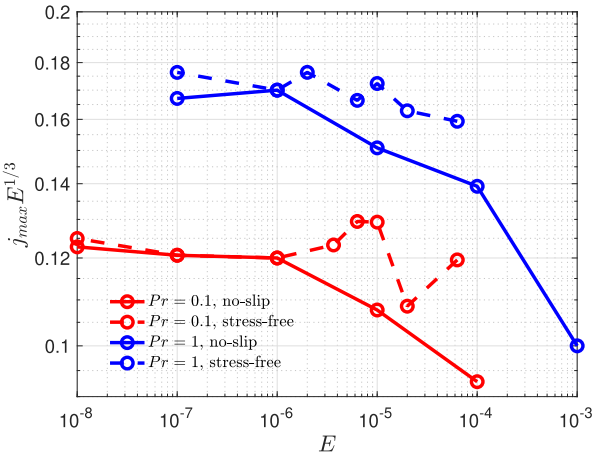

Figure 9. Spectral peak for the onset modes, scaled by $E^{1/3}$. The quantity j_{max} is the index at which the stream-function spectra $|c_j|$ reaches its maximum value. The colours refer to the Pr number for which the solution is calculated. Full and dashed lines indicate, respectively, no-slip and stress-free calculations.

equatorially symmetric component of the temperature field, and no information on the asymmetric part enters the PG equations. In line with the magnetic moments derived in Paper 1, the diffusion-free part of the evolution equations for $\overline{T}$ and $\widetilde{zT}$ is derived without the need of further assumptions or approximations. The resulting mathematical form of thermal diffusion, however, is not closed in these thermal moments, and additional manipulation is required. In order to keep the system closed in the PG variables Ψ, $\overline{T}$ and $\widetilde{zT}$, we chose to adopt an approximated form for thermal diffusion, based on the assumption that the spatial derivatives along the vertical direction are of smaller magnitude than the ones along the equatorial directions. The validity of this approximation has been corroborated via 3-D calculations (see Fig. 4).

We also developed a framework for numerical studies based on the PG equations. The methodology of choice is fully spectral, due to the superior convergence properties of these methods in the regular domain geometries we are interested in (Boyd 2001). All PG variables are discretized via a Galerkin basis set and the expansion coefficients are found via integration. This choice is mostly guided by the weak-form nature of the stress-free viscous correction, and it further allows us to treat the singularity of the no-slip correction, which is integrable in our framework. A peculiar aspect of our numerical implementation is the need to resort to the Gauss–Jacobi quadrature for numerical calculation of the resulting integral, at least for the no-slip implementation. This is due to the mathematical form of the Ekman pumping term, which cannot be integrated via the more commonly used Gauss–Chebyshev method. The drawback of the Gauss–Jacobi rule is the need to numerically find the zeros of a set of Jacobi polynomials, for which no closed form exists. Although we did not extensively validate the calculation of quadrature nodes and weights in our implementation, we find that the final integration results is correct to at least machine precision in our calculations. We ascertained that by (i) comparing the mass matrices of the numerical system (eqs 37–39), $\mathcal{N}$, $\overline{\mathcal{C}}$, $\widetilde{\mathcal{C}}$, always calculated numerical within our framework, with unit matrices and (ii) sporadically comparing the numerical calculation of high-order terms in the right-hand side integrals of eqs (37)–(39) with analytical calculations, possible with `Mathematica`.

The PG hydrothermal equations (eqs 10, 19 and 20), and the numerical methodology of choice, have been benchmarked on the problem of the onset of thermal convection in a sphere. Our PG calculations were compared with 3-D and columnar-flow calculations made with a state-of-the-art columnar-flow model (Guervilly & Cardin 2016), referred to as the QG-Hyb model. This comparison proved the validity of our PG methodology. In particular we found that, both in terms of reproducing known 3-D onset values and in terms of reaching the expected asymptotic regimes at low-E values, our PG model performs generally better than the QG-Hyb model.

In this work, we expanded the velocity field as a sum of inviscid inertial waves (see eq. 31). A similar methodology is routinely used by Zhang and colleagues in 3-D convection studies (e.g. Zhang & Liao 2004; Zhang *et al.* 2007, 2017). This specific choice results in zero diagonal terms in the dissipation integrals (eqs 48 and 53). Physically, this means that internal self-dissipation of the basis set of choice is null, in agreement with the fact that the basis elements are solution to the inviscid momentum equation. The onset of thermal convection,

however, is intrinsically viscous in nature, and the absence of internal dissipation makes the problem physically ill-posed. The inclusion of no-slip and stress-free corrections introduces non-zero diagonal terms, rendering the problem physically well-posed and in agreement with the viscous dissipation acting primarily through the boundary layers for the moderate-to-low Pr numbers and low E numbers of interest in typical geophysical applications (Zhang 1994, 1995; Zhang & Liao 2017). In contrast, the asymptotic analysis illustrated in Section 4.2 does not require neither the stress-free nor the no-slip boundary condition, but a physical solution is nevertheless obtained, since no specific stream-function expansion is needed.

In this work, we have ignored the presence of magnetic effects, since our goal was focussed on the purely hydrodynamic aspects of the PG system. From our non-magnetic investigation, we retrieved the critical values for the onset of thermal convection, most importantly, Ra_c. These values will inform future non-linear simulations, since supercriticality (the ratio Ra/Ra_c) is one of the most important input parameters in thermally driven magneto-hydrodynamic simulations. For fixed values of the other input parameters, such as E and Pr, supercriticality sets, for example, the magnitude of the convective flows and their spatial properties (Guervilly *et al.* 2019), the heat transferred outside of the domain, and the generation of axisymmetric, zonal flows (Aubert *et al.* 2003; Barrois *et al.* 2022). In the PG framework, the latter can be modelled by adding a separate equation for the axisymmetric motions, obtained by taking the geostrophic average of the momentum eq. (1), as done in other columnar-flow implementations (e.g. Aubert *et al.* 2003; Guervilly & Cardin 2016; Barrois *et al.* 2022). Zonal winds would then arise from non-linear interaction of the non-zonal flows.

Magnetic effects, important in the dynamics of Earth's outer core, can be reinstated in the hydro-thermal PG eqs (10)–(20), by adding terms derived from the Lorentz force in the momentum eq. (10) and by considering the temporal evolution of the magnetic moments, as done in Paper 1. The final major ingredient to be implemented is magnetic diffusion. The insights gained in the derivation of approximated thermal diffusion eqs (22) and (23) will be certainly invaluable to that end, but magnetic diffusion presents challenges of its own. The assumptions that temperature is characterized by low vertical complexity, used in the derivation of eqs (22) and (23), is supported in recent geodynamo simulations (e.g. Schaeffer *et al.* 2017; Aubert 2019), the same simulations suggest that the magnetic field possesses a much higher spatial complexity. Furthermore the magnetic field is considered via quadratic quantities in the PG framework (Paper 1), resulting in further mathematical challenges. By comparison, the bulk viscous term in the momentum equation, F_V in eq. (10) does not present the same difficulties in its implementation. The Laplacian term, $\nabla^2\mathbf{u}$ involved in the calculation of F_V, is in fact closed in the relevant PG variable, Ψ, due to the columnar-flow assumption (eq. 9) and no additional approximation or simplification is therefore required to obtain closure.

Finally we point out that the numerical code developed for the calculations of the results presented in this study is not optimized for performance on modern supercomputers. Our code was primarily intended as a test-bed in which the methodology illustrated in this study could be tested. The choice of `Mathematica` was guided primarily by the need to carefully test our algorithms, facilitated by the simplicity of the language, the ease of implementation of analytical calculations and the ease of access to vast libraries to, for example, solve eigenvalue problems. Work is ongoing to implement the PG equation via programming environment better suited for high-performance computational studies.

AUTHOR CONTRIBUTIONS

Stefano Maffei (Conceptualization, Formal analysis, Funding acquisition, Investigation, Methodology, Project administration, Software, Writing–original draft); Andrew Jackson (Conceptualization, Formal analysis, Funding acquisition, Investigation, Methodology, Project administration, Writing–original draft); Philip W. Livermore (Conceptualization, Formal analysis, Investigation, Methodology, Writing–original draft).

ACKNOWLEDGMENTS

This project has been funded by ESA in the framework of EO Science for Society, through contract No. 4000138930/22/I-DT-bgh (Core Dynamics & Data Assimilation: Fundamentals). We are also grateful for funding from the European Research Council (agreement no. 833848-UEMHP) under the Horizon 2020 programme, and from the Swiss National Science Foundation (MINT project no. 219247). Numerical calculations were performed on the ETH Zürich Euler cluster.

DATA AVAILABILITY

A `Mathematica` notebook that can be used to reproduce the PG model results presented in this paper is freely available from the Github repository https://github.com/smaffei/PG-basics.git. The notebook can be used to generate the PG matrices and calculate both the viscous corrections and the critical values at the onset of thermal convection.

Published values for onset of thermal convection in a full sphere have been taken from Jones *et al.* (2000); Zhang *et al.* (2004, 2007); Zhang & Liao (2017), for 3-D calculations, and from Guervilly & Cardin (2016), for the QG-Hyb model.

The code `QuICC`, used to complement the above-mentioned 3-D calculations is available at https://github.com/QuICC. Access can be granted upon contacting the repository administrator, Dr Philippe Marti (ETH Zurich). For this study, the version of the `QuICC` framework used is `onset_v0.1.0`, and the specific physical model is the `BoussinesqSphereRTC` version `v1.12.0`.

REFERENCES

Arfken, G.B., Weber, H.-J. & Harris, F.E., 2011. *Mathematical Methods for Physicists: A Comprehensive Guide,* 7th edn, Academic Press.

Aubert, J., 2019. Approaching Earth's core conditions in high-resolution geodynamo simulations, *Geophys. J. Int.,* **219**(Suppl. 1), S137–S151.

Aubert, J., 2023. State and evolution of the geodynamo from numerical models reaching the physical conditions of Earth's core, *Geophys. J. Int.,* **235**(1), 468–487.

Aubert, J., Gillet, N. & Cardin, P., 2003. Quasigeostrophic models of convection in rotating spherical shells, *Geochem. Geophys. Geosyst.,* **4**(7), doi:10.1029/2002GC000456.

Aubert, J., Gastine, T. & Fournier, A., 2017. Spherical convective dynamos in the rapidly rotating asymptotic regime, *J. Fluid Mech.,* **813,** 558–593.

Aubert, J., Livermore, P.W., Finlay, C.C., Fournier, A. & Gillet, N., 2022. A taxonomy of simulated geomagnetic jerks, *Geophys. J. Int.,* **231**(1), 650–672.

Backus, G., Parker, R.L. & Constable, C., 1996. *Foundations of Geomagnetism,* Cambridge Univ. Press.

Baer, M., 2018. *findiff software package.,* https://github.com/maroba/findiff.

Barrois, O., Gastine, T. & Finlay, C.C., 2022. Comparison of quasi-geostrophic, hybrid and 3-D models of planetary core convection, *Geophys. J. Int.,* **231**(1), 129–158.

Boyd, J.P., 2001. *Chebyshev and Fourier Spectral Methods,* Courier Dover Publications.

Busse, F.H., 1970. Thermal instabilities in rapidly rotating systems, *J. Fluid Mech,* **44**(3), 441–460.

Calkins, M.A., Noir, J., Eldredge, J.D. & Aurnou, J.M., 2012. The effects of boundary topography on convection in Earth's core, *Geophys. J. Int.,* **189**(2), 799–814.

Calkins, M.A., Orvedahl, R.J. & Featherstone, N.A., 2021. Large-scale balances and asymptotic scaling behaviour in spherical dynamos, *Geophys. J. Int.,* **227**(2), 1228–1245.

Canet, E., Fournier, A. & Jault, D., 2009. Forward and adjoint quasi-geostrophic models of the geomagnetic secular variation, *J. geophys. Res.,* **114**(B11), doi:10.1029/2008JB006189.

Canet, E., Finlay, C.C. & Fournier, A., 2014. Hydromagnetic quasi-geostrophic modes in rapidly rotating planetary cores, *Phys. Earth planet. Inter.,* **229,** 1–15.

Cardin, P. & Olson, P., 1994. Chaotic thermal convection in a rapidly rotating spherical shell: consequences for flow in the outer core, *Phys. Earth planet. Inter.,* **82**(3–4), 235–259.

Chandrasekhar, S., 1961. *Hydrodynamic and Hydromagnetic Stability,* Courier Corporation.

Charney, J.G., 1948. On the scale of atmospheric motions, *Geofysiske Publikasjoner,* **17**(2), 251–265.

Chaskalovic, J. & Chaskalovic, J., 2008. *Finite Element Methods for Engineering Sciences: Theoretical Approach and Problem Solving Techniques,* Springer Science & Business Media.

Cheng, J.S., Madonia, M., Aguirre Guzmán, A.J. & Kunnen, R.P.J., 2020. Laboratory exploration of heat transfer regimes in rapidly rotating turbulent convection, *Phys. Rev. Fluids,* **5,** doi:10.1103/PhysRevFluids.5.113501.

Christensen, U.R. & Wicht, J., 2015. 8.10 - Numerical dynamo simulations, in *Treatise on Geophysics,* 2nd edn, pp. 245–277, ed. Schubert, G., Elsevier.

Davidson, P.A., 2013. *Turbulence in Rotating, Stratified and Electrically Conducting Fluids,* Cambridge Univ. Press.

Dumberry, M. & More, C., 2020. Weak magnetic field changes over the Pacific due to high conductance in lowermost mantle, *Nat. Geosci.,* **13**(7), 516–520.

Gerick, F., Jault, D., Noir, J. & Vidal, J., 2020. Pressure torque of torsional Aalfvén modes acting on an ellipsoidal mantle, *Geophys. J. Int.,* **222**(1), 338–351.

Gerick, F., Jault, D. & Noir, J., 2021. Fast quasi-geostrophic Magneto-Coriolis modes in the Earth's core, *Geophys. Res. Lett.,* **48**(4), e2020GL090803.

Gillet, N. & Jones, C.A., 2006. The quasi-geostrophic model for rapidly rotating spherical convection outside the tangent cylinder, *J. Fluid Mech.,* **554,** 343–369.

Gillet, N., Schaeffer, N. & Jault, D., 2011. Rationale and geophysical evidence for quasi-geostrophic rapid dynamics within the Earth's outer core, *Phys. Earth planet. Inter.,* **202–203,** 78–88.

Gillet, N., Gerick, F., Jault, D., Schwaiger, T., Aubert, J. & Istas, M., 2022. Satellite magnetic data reveal interannual waves in Earth's core, *Proc. Natl. Acad. Sci.,* **119**(13), e2115258119.

Greenspan, H.P., 1968. *The Theory of Rotating Fluids,* CUP Archive.

Guervilly, C. & Cardin, P., 2016. Subcritical convection of liquid metals in a rotating sphere using a quasi-geostrophic model, *J. Fluid Mech.,* **808,** 61–89.

Guervilly, C., Cardin, P. & Schaeffer, N., 2019. Turbulent convective length scale in planetary cores, *Nature,* **570**(7761), 368–371.

Hildebrand, F.B., 1987. *Introduction to Numerical Analysis,* Courier Corporation.

Holme, R., 2015. 8.04 - Large-scale flow in the core, in *Treatise on Geophysics,* 2nd edn, pp. 91–113, ed. Schubert, G., Elsevier.

Jackson, A. & Maffei, S., 2020. Plesio-geostrophy for Earth's core: I. Basic equations, inertial modes and induction, *Proc. R. Soc., A,* **476**(2243),doi:10.1098/rspa.2020.0513 (Paper 1).

Jault, D., 2008. Axial invariance of rapidly varying diffusionless motions in the Earth's core interior, *Phys. Earth planet. Inter.,* **166**(1–2), 67–76.

Jones, C., 2015. 8.05 - Thermal and compositional convection in the outer core, in *Treatise on Geophysics,* 2nd edn, pp. 115–159, ed. Schubert, G., Elsevier.

Jones, C.A., Soward, A.M. & Mussa, A.I., 2000. The onset of thermal convection in a rapidly rotating sphere, *J. Fluid Mech.,* **405,** 157–179.

Julien, K., Knobloch, E., Milliff, R. & Werne, J., 2006. Generalized quasi-geostrophy for spatially anisotropic rotationally constrained flows, *J. Fluid Mech.,* **555,** 233–274.

Kida, S., 2011. Steady flow in a rapidly rotating sphere with weak precession, *J. Fluid Mech.,* **680,** 150–193.

Kudlick, M.D., 1966. On transient motions in a contained, rotating fluid, *PhD thesis*, MIT, Department of Mathematics.

Kunnen, R.P.J., Geurts, B.J. & Ckercx, H.J.H., 2010. Experimental and numerical investigation of turbulent convection in a rotating cylinder, *J. Fluid Mech.,* **642,** 445–476.

Labbé, F., Jault, D. & Gillet, N., 2015. On magnetostrophic inertia-less waves in quasi-geostrophic models of planetary cores, *Geophys. Astrophys. Fluid Dyn.,* **109**(6), 587–610.

Landeau, M., Fournier, A., Nataf, H.-C., Cébron, D. & Schaeffer, N., 2022. Sustaining Earth's magnetic dynamo, *Nat. Rev. Earth Environ.,* **3**(4), 255–269.

Lewis, H.R. & Bellan, P.M., 1990. Physical constraints on the coefficients of Fourier expansions in cylindrical coordinates, *J. Math. Phys.,* **31**(11), 2592–2596.

Li, K., Livermore, P.W. & Jackson, A., 2010. An optimal Galerkin scheme to solve the kinematic dynamo eigenvalue problem in a full sphere, *J. Comput. Phys.,* **229**(23), 8666–8683.

Liao, X. & Zhang, K., 2008. On viscous decay factors for spherical inertial modes in rotating planetary fluid cores: comparison between asymptotic and numerical analysis, *Phys. Earth planet. Inter.,* **169**(1–4), 211–219.

Liao, X., Zhang, K. & Earnshaw, P., 2001. On the viscous damping of inertial oscillation in planetary fluid interiors, *Phys. Earth planet. Inter.,* **128**(1–4), 125–136.

Lin, Y., Marti, P., Noir, J. & Jackson, A., 2016. Precession-driven dynamos in a full sphere and the role of large scale cyclonic vortices, *Phys. Fluids,* **28**(6), doi: 10.1063/1.4954295.

Long, R.S., Mound, J.E., Davies, C.J. & Tobias, S.M., 2020. Scaling behaviour in spherical shell rotating convection with fixed-flux thermal boundary conditions, *J. Fluid Mech.,* **889,** A7, doi:10.1017/jfm.2020.67.

Maffei, S. & Jackson, A., 2016. Propagation and reflection of diffusionless torsional waves in a sphere, *Geophys. J. Int.,* **204**(3), 1477–1489.

Maffei, S., Jackson, A. & Livermore, P.W., 2017. Characterization of columnar inertial modes in rapidly rotating spheres and spheroids, *Proc. R. Soc. A,* **473**(2204), doi:10.1098/rspa.2017.0181.

Marti, P. & Jackson, A., 2021. Accurate and efficient jones-worland spectral transforms for planetary applications, in *PASC'21: Proceedings of the Platform for Advanced Scientific Computing Conference,* Geneva, Switzerland, 5–9 July 2021, Association for Computing Machinery.
Marti, P. *et al.*, 2014. Full sphere hydrodynamic and dynamo benchmarks, *Geophys. J. Int.,* **197**(1), 119–134.
Marti, P., Calkins, M.A. & Julien, K., 2016. A computationally efficient spectral method for modeling core dynamics, *Geochem. Geophys. Geosyst.,* **17**(8), 3031–3053.
More, C. & Dumberry, M., 2017. Convectively driven decadal zonal accelerations in Earth's fluid core, *Geophys. J. Int.,* **213**(1), 434–446.
Rajaei, H., Alards, K. M.J., Kunnen, R. P.J. & Clercx, H. J.H., 2018. Velocity and acceleration statistics in rapidly rotating Rayleigh–BéNard convection, *J. Fluid Mech.,* **857,** 374–397.
Roberts, P., 1965. On the thermal instability of a highly rotating fluid sphere., *Astrophys. J.,* **141,** 240, doi:10.1086/148106.
Roberts, P.H., 1968. On the thermal instability of a rotating-fluid sphere containing heat sources, *Phil. Trans. R. Soc. Lond., A,* **263**(1136), 93–117.
Roberts, P.H. & Stewartson, K., 1963. On the stability of a maclaurin spheroid of small viscosity, *Astrophys. J.,* **137,** 777, doi:10.1086/147555.
Schaeffer, N., 2004. Instabilités, turbulence et dynamo dans une couche de fluide cisaillée en rotation rapide. Importance de l'aspect ondulatoire, *PhD thesis*, Université Joseph-Fourier-Grenoble I.
Schaeffer, N. & Cardin, P., 2005a. Quasigeostrophic model of the instabilities of the Stewartson layer in flat and depth-varying containers, *Phys. Fluids,* **17**(10), doi:10.1063/1.2073547.
Schaeffer, N. & Cardin, P., 2005b. Rossby-wave turbulence in a rapidly rotating sphere, *Nonlin. Process. Geophys.,* **12**(6), 947–953.
Schaeffer, N., Silva, E.L. & Pais, M.A., 2016. Can core flows inferred from geomagnetic field models explain the Earth's dynamo?, *Geophys. J. Int.,* **204**(2), 868–877.
Schaeffer, N., Jault, D., Nataf, H.-C. & Fournier, A., 2017. Turbulent geodynamo simulations: a leap towards Earth's core, *Geophys. J. Int.,* **211**(1), 1–29.
Shchepetkin, A.F. & O'Brien, J.J., 1996. A physically consistent formulation of lateral friction in shallow-water equation ocean models, *Mon. Wea. Rev.,* **124**(6), 1285–1300.
Sheyko, A., 2014. .Numerical investigations of rotating MHD in a spherical shell, *Doctoral thesis*, ETH-Zürich.
Sheyko, A., Finlay, C.C. & Jackson, A., 2016. Magnetic reversals from planetary dynamo waves, *Nature,* **539**(7630), 551–554.
Sheyko, A., Finlay, C., Favre, J. & Jackson, A., 2018. Scale separated low viscosity dynamos and dissipation within the Earth's core, *Sci. Rep.,* **8**(1), doi:10.1038/s41598-018-30864-1.
Wicht, J. & Sanchez, S., 2019. Advances in geodynamo modelling, *Geophys. Astrophys. Fluid Dyn.,* **113**(1–2), 2–50.
Zhang, K., 1992. Spiralling columnar convection in rapidly rotating spherical fluid shells, *J. Fluid Mech.,* **236,** 535–556.
Zhang, K., 1994. On coupling between the Poincaré equation and the heat equation, *J. Fluid Mech.,* **268,** 211–229.
Zhang, K., 1995. On coupling between the Poincaré equation and the heat equation: non-slip boundary condition, *J. Fluid Mech.,* **284,** 239–256.
Zhang, K. & Jones, C.A., 1993. The influence of Ekman boundary layers on rotating convection, *Geophys. Astrophys. Fluid Dyn.,* **71**(1–4), 145–162.
Zhang, K. & Liao, X., 2004. A new asymptotic method for the analysis of convection in a rapidly rotating sphere, *J. Fluid Mech.,* **518,** 319–346.
Zhang, K. & Liao, X., 2017. *Theory and Modeling of Rotating Fluids: Convection, Inertial Waves and Precession, Cambridge Monographs on Mechanics,* Cambridge Univ. Press.
Zhang, K., Earnshaw, P., Liao, X. & Busse, F.H., 2001. On inertial waves in a rotating fluid sphere, *J. Fluid Mech.,* **437,** 103–119.
Zhang, K., Liao, X. & Earnshaw, P., 2004. On inertial waves and oscillations in a rapidly rotating spheroid, *J. Fluid Mech.,* **504,** 1–40.
Zhang, K., Liao, X. & Busse, F.H., 2007. Asymptotic solutions of convection in rapidly rotating non-slip spheres, *J. Fluid Mech.,* **578,** 371–380.
Zhang, K., Lam, K. & Kong, D., 2017. Asymptotic theory for torsional convection in rotating fluid spheres, *J. Fluid Mech.,* **813,** doi:10.1017/jfm.2017.9.

APPENDIX A: GENERAL FORM OF THE CORIOLIS TERM

In this Appendix we derive a generic form of the Coriolis term F_C that appears in the PG momentum eq. (10). We set:

$$\mathbf{f} = -2\hat{\mathbf{z}} \times \mathbf{v}$$

but we do not assume that the velocity $\mathbf{v}$ has a columnar structure, nor do we specify the boundary conditions. We do, however, assume that the flow is incompressible: $\nabla \times \mathbf{v} = 0$. Applying formula (11) we obtain:

$$F_C = 4\frac{dH}{ds} v_s|_0 - 2\hat{\mathbf{z}} \cdot \nabla \times (\hat{\mathbf{z}} \times \overline{\mathbf{v}_e}).$$

The second term can be manipulated using well known vector calculus identities:

$$-2\hat{\mathbf{z}} \cdot \nabla \times (\hat{\mathbf{z}} \times \overline{\mathbf{v}_e}) = -2\hat{\mathbf{z}} \cdot [\hat{\mathbf{z}}(\nabla \cdot \overline{\mathbf{v}_e}) - \overline{\mathbf{v}_e}(\nabla \cdot \hat{\mathbf{z}}) + (\overline{\mathbf{v}_e} \cdot \nabla)\hat{\mathbf{z}} - (\hat{\mathbf{z}} \cdot \nabla)\overline{\mathbf{v}_e}] = -2\nabla \cdot \overline{\mathbf{v}_e} \tag{A1}$$

In writing the last identity, we used the fact that the spatial derivatives of the unit vector $\hat{\mathbf{z}}$ are identically zero, and that $\overline{\mathbf{v}_e}$, a vertically integrated quantity, does not depend on z. Further progress is made by explicitly expanding the divergence operator in cylindrical coordinates and making use of the Leibniz integration rule:

$$\begin{aligned} -2\nabla \cdot \overline{\mathbf{v}_e} &= -2\left(\frac{\partial \overline{v_s}}{\partial s} + \frac{1}{s}\overline{v_s} + \frac{1}{s}\frac{\partial \overline{v_\phi}}{\partial \phi}\right) = -2\left[\overline{\left(\frac{\partial v_s}{\partial s} + \frac{1}{s}v_s + \frac{1}{s}\frac{\partial v_\phi}{\partial \phi}\right)} + \frac{dH}{ds}(v_s|_H + v_s|_{-H})\right] \\ &= -2\left[-\overline{\frac{\partial v_z}{\partial z}} + \frac{dH}{ds}(v_s|_H + v_s|_{-H})\right] = -2\left[-(v_z|_H - v_z|_{-H}) + \frac{dH}{ds}(v_s|_H + v_s|_{-H})\right]. \end{aligned}$$

On the upper and lower hemispheres of the unit sphere, defined, respectively, by $z = +H$ and $z = -H$, we have:

$$\begin{aligned} v_r|_H &= s v_s|_H + H v_z|_H \\ v_r|_{-H} &= s v_s|_{-H} - H v_z|_{-H}. \end{aligned}$$

Since $\mathrm{d}H/\mathrm{d}s = -sH^{-1}$:

$$F_C = -4\frac{s}{H}v_s|_0 + \frac{2}{H}\left(v_r|_H + v_r|_{-H}\right),$$

which is formula (43)

APPENDIX B: NO-SLIP CORRECTION

Here we illustrate some details on the viscous correction arising from the application of no-slip boundary conditions via Ekman pumping. We start by illustrating how the singular behaviour arises from eq. (42). Let us first define:

$$P_1 = \frac{1}{2\sqrt{H}}\left(-\frac{s}{2H}u_\phi\right),$$
$$P_2 = \frac{1}{2\sqrt{H}}\left(-\frac{5}{2}\frac{s}{H^2}u_s\right),$$
$$P_3 = \frac{1}{2\sqrt{H}}\left(-H\omega_z\right),$$
$$P_4 = \frac{1}{2\sqrt{H}}\left(\frac{s}{H}\frac{\partial u_s}{\partial\phi}\right).$$

such that $u_{1r}|_{z=\pm H} = E^{1/2}(P_1 + P_2 + P_3 + P_4)$. Making use of eqs (9) and (31) it is possible to show that:

$$P_1 = -\frac{1}{4}s^m H^{-3/2}\left[\left(m\left(s^2-1\right)+3s^2\right)p_j(s) + s\left(s^2-1\right)p_j'(s)\right]\mathrm{e}^{\mathrm{i}m\phi},$$
$$P_2 = -\frac{5}{4}\mathrm{i}ms^m H^{-1/2}p_j(s)\mathrm{e}^{\mathrm{i}m\phi},$$
$$P_3 = -\frac{1}{2}s^m H^{1/2}\left[(5m+6)p_j(s) + \left(-2mH^2+6s^2-1\right)s^{-1}p_j'(s) - H^2p_j''(s)\right]\mathrm{e}^{\mathrm{i}m\phi},$$
$$P_4 = -\frac{1}{2}m^2s^m H^{1/2}p_j(s)\mathrm{e}^{\mathrm{i}m\phi}.$$

where $p_j(s) = P_{j-1}^{(3,m-1/2)}(2s^2-1)$ for brevity and generality. Note that $s^{-1}p'(s)$ is not singular for $s \to 0$, since $p(s)$ is a regular polynomial in s^2. Focussing on the behaviour as $s \to 1$, the above identities show that $u_{1r}|_{z=\pm H} \sim H^{-3/2}$.

Inserting the above identities into eq. (45) we obtain the following integrals:

$$\Pi_{ij}^{(1)} = -\frac{1}{2}\int_0^{2\pi}\int_0^1 s^{2m+1}H^{-1/2}p_i(s)\left[\left(m\left(s^2-1\right)+3s^2\right)p_j(s) + s\left(s^2-1\right)p_j'(s)\right]ds\,d\phi,$$
$$\Pi_{ij}^{(2)} = -\mathrm{i}m\frac{5}{2}\int_0^{2\pi}\int_0^1 s^{2m+1}H^{1/2}p_i(s)p_j(s)ds\,d\phi,$$
$$\Pi_{ij}^{(3)} = -\int_0^{2\pi}\int_0^1 s^{2m+1}H^{3/2}p_i(s)\left[(5m+6)p_j(s) + \left(-2mH^2+6s^2-1\right)s^{-1}p_j'(s) - H^2p_j''(s)\right]ds\,d\phi,$$
$$\Pi_{ij}^{(4)} = -m^2\int_0^{2\pi}\int_0^1 s^{2m+1}H^{3/2}p_i(s)p_j(s)ds\,d\phi,$$

such that $\Sigma_{ij}^{ns} = \Pi_{ij}^{(1)} + \Pi_{ij}^{(2)} + \Pi_{ij}^{(3)} + \Pi_{ij}^{(4)}$. The only singularity is now contained in the integrand of $\Pi_{ij}^{(1)}$, and it is integrable.

We finally comment on the quadrature rules necessary to calculate the above integrals. As discussed in Section 3, the radial part of the above integrals can generally be calculated via Gauss–Jacobi quadrature. Upon performing the substitution $x = 2s^2 - 1$, we can transform the above integrals in the form required by the quadrature rule (eq. 52). It can be shown that the quadrature's α and β for the above integrals are, respectively, $\alpha = -1/4; 1/4; 3/4; 3/4$, and $\beta = m$ for all of them. Integrals $\Pi_{ij}^{(3)}$ and $\Pi_{ij}^{(4)}$ can therefore be treated in the same manner. Note also that there is no single quadrature rule that is exact for all of the above integrals. That is because the pre-factor of H always appears with a half-integer power. Specifically, the rule valid for $\Pi_{ij}^{(1)}$ can be applied to $\Pi_{ij}^{(3)}$ and $\Pi_{ij}^{(4)}$, by increasing the degree of the polynomial $f(x)$, but not to $\Pi_{ij}^{(2)}$, since the resulting $f(x)$ would not be a polynomial, and the quadrature rule would not be exact anymore.

APPENDIX C: STRESS-FREE CORRECTION

In principle the stress-free conditions (eq. 8) apply to the total flow $\mathbf{v}$, defined here as in eq. (41):

$$\mathbf{v} = \mathbf{u} + \mathbf{u}_1, \tag{C1}$$

where $\mathbf{u}$ is the interior, columnar and inviscid flow described by the columnar flow formalism (eq. 9) and $||\mathbf{u}_1|| \ll ||\mathbf{u}||$ is a correction that ensures that the tangential conditions (eq. 8) are satisfied. In particular, it is possible to show that $\mathbf{u}_1$ is proportional to E (see for example Zhang 1994; Liao *et al.* 2001). We further assume that the total flow $\mathbf{v}$ satisfies incompressibility, $\nabla\cdot\mathbf{v} = 0$.

To implement the stress-free boundary conditions in the PG framework we follow the procedure outlined in Maffei *et al.* (2017), where we considered the columnar-flow implementation first presented in Labbé *et al.* (2015). In the PG framework, the mathematical details are more complicated and we illustrate them below. In the weak formulation we multiply the momentum eq. (10) by Ψ^*, a weight function w_Ψ (for generality), and integrate in s and ϕ. The PG viscous term, in its weak form, is, as in eq. (48):

$$\mathcal{G} = \int_{disc} \Psi^* \frac{s}{2H} F_V \, w_\Psi \, ds d\phi$$

Let us introduce the following notation:

$$\nabla^2 \mathbf{v} \equiv \mathbf{L},$$

so that:

$$\widetilde{\hat{\mathbf{z}} \cdot \nabla^2 \mathbf{v}} \equiv \widetilde{L_z},$$
$$\overline{(\nabla^2 \mathbf{v})_e} \equiv \overline{\mathbf{L}_e},$$
$$\hat{\boldsymbol{\phi}} \cdot \nabla^2 \mathbf{v}|_0 \equiv L_\phi|_0.$$

Furthermore, we indicate the vorticity with $\boldsymbol{\omega} = \nabla \times \mathbf{v}$. The integral (eq. 48) can then be expanded as:

$$\begin{aligned}\mathcal{G} &= \int_{disc} \Psi^* \frac{s}{2H} \left\{ \frac{dH}{ds} \left[-\frac{1}{s} \frac{\partial \widetilde{L_z}}{\partial \phi} - 2L_\phi|_0 \right] + \hat{\mathbf{z}} \cdot \nabla \times \overline{\mathbf{L}_e} \right\} w_\Psi ds d\phi \\ &= \underbrace{\int_{disc} \Psi^* \frac{s}{2H} \frac{dH}{ds} \left[-\frac{1}{s} \frac{\partial \widetilde{L_z}}{\partial \phi} \right] w_\Psi ds d\phi}_{\equiv \widetilde{\mathcal{G}}} + \underbrace{\int_{disc} \Psi^* \frac{s}{2H} \frac{dH}{ds} \left[-2L_\phi|_0 \right] w_\Psi ds d\phi}_{\equiv \mathcal{G}_0} + \underbrace{\int_{disc} \Psi^* \frac{s}{2H} \hat{\mathbf{z}} \cdot \nabla \times \overline{\mathbf{L}_e} w_\Psi ds d\phi}_{\equiv \overline{\mathcal{G}}}.\end{aligned}$$

As illustrated in the above, the full integral $\mathcal{G}$ is then decomposed as a sum of three terms: $\widetilde{\mathcal{G}}$, $\overline{\mathcal{G}}$, $\mathcal{G}_0$.

Let us consider the $\overline{\mathcal{G}}$ term. By making use of the Leibniz integration rule:

$$\begin{aligned}\overline{\mathcal{G}} &= \int_{disc} \Psi^* \frac{s}{2H} \hat{\mathbf{z}} \cdot \nabla \times \int_{-H}^{H} \mathbf{L_e} dz \, w_\Psi ds d\phi = \int_{disc} \Psi^* \frac{s}{2H} \left[\int_{-H}^{H} \hat{\mathbf{z}} \cdot \nabla \times \mathbf{L_e} dz - \frac{2s}{H} L_\phi \right] w_\Psi ds d\phi \\ &= \int_{core} \Psi^* \frac{1}{2H} \hat{\mathbf{z}} \cdot \nabla \times \mathbf{L} \, w_\Psi dV - \int_{disc} \Psi^* \frac{s}{H^2} L_\phi \, w_\Psi dA,\end{aligned}$$

where $\mathrm{d}A = s \mathrm{d}\phi \mathrm{d}s$ is the surface area element on the equatorial disc. In the above we assumed that $L_\phi|_H = L_\phi|_{-H} = L_\phi$. We recognize the second integral in the above to be equivalent to $-\mathcal{G}_0$ (since, in the interior of the domain, $L_\phi|_0 = L_\phi$), so:

$$\overline{\mathcal{G}} + \mathcal{G}_0 = \int_{core} \Psi^* \frac{1}{2H} \hat{\mathbf{z}} \cdot \nabla \times \mathbf{L} \, w_\Psi dV = \int_{core} \nabla \times \left[\Psi^* \frac{w_\Psi}{2H} \hat{\mathbf{z}} \right] \cdot \mathbf{L} \, dV - \int_{core} \nabla \cdot \left[\Psi^* \frac{w_\Psi}{2H} \hat{\mathbf{z}} \times \mathbf{L} \right] dV$$

The remaining integral is:

$$\widetilde{\mathcal{G}} = \int_{disc} \Psi^* \frac{w_\Psi}{2H} \frac{s}{H} \left[\frac{1}{s} \frac{\partial \widetilde{L_z}}{\partial \phi} \right] s ds d\phi = -\int_{disc} \frac{\partial \Psi^*}{\partial \phi} \frac{w_\Psi}{2H^2} \widetilde{L_z} dA = -\int_{core} \frac{\partial \Psi^*}{\partial \phi} \frac{w_\Psi}{2H^2} \mathrm{sgn}(z) \hat{\mathbf{z}} \cdot \mathbf{L} \, dV.$$

Let us now sum the terms back together:

$$\begin{aligned}\overline{\mathcal{G}} + \mathcal{G}_0 + \widetilde{\mathcal{G}} &= \int_{core} \nabla \times \left[\Psi^* \frac{w_\Psi}{2H} \hat{\mathbf{z}} \right] \cdot \mathbf{L} \, dV - \int_{core} \nabla \cdot \left[\Psi^* \frac{w_\Psi}{2H} \hat{\mathbf{z}} \times \mathbf{L} \right] dV - \int_{core} \frac{\partial \Psi^*}{\partial \phi} \frac{w_\Psi}{2H^2} \mathrm{sgn}(z) \hat{\mathbf{z}} \cdot \mathbf{L} \, dV \\ &= \int_{core} \underbrace{\left\{ \nabla \times \left[\Psi^* \frac{w_\Psi}{2H} \hat{\mathbf{z}} \right] - \frac{\partial \Psi^*}{\partial \phi} \frac{w_\Psi}{2H^2} \mathrm{sgn}(z) \hat{\mathbf{z}} \right\}}_{\equiv \mathbf{U}^*} \cdot \mathbf{L} \, dV - \int_{core} \nabla \cdot \left[\Psi^* \frac{w_\Psi}{2H} \hat{\mathbf{z}} \times \mathbf{L} \right] dV.\end{aligned}$$

In the above we have introduced the complex conjugate, pseudo-velocity $\mathbf{U}^*$, in order to simplify the remainder of the derivation. The first integral can be manipulated as in Zhang (1994) and Maffei *et al.* (2017):

$$\begin{aligned}\int_{core} \mathbf{U}^* \cdot \mathbf{L} \, dV &= \int_{core} \mathbf{U}^* \cdot \nabla^2 \mathbf{v} \, dV = -\int_{core} \nabla \times \mathbf{U}^* \cdot \nabla \times \mathbf{v} \, dV + \oint_{CMB} \hat{\boldsymbol{r}} \cdot (\mathbf{U}^* \times \nabla \times \mathbf{v}) \, d\Omega \\ &= -\int_{core} \nabla \times \mathbf{U}^* \cdot \nabla \times \mathbf{v} \, dV + \oint_{CMB} \left[2(U_\theta^* v_\theta + U_\phi^* v_\phi) + U_\theta^* \frac{\partial}{\partial r} \left(\frac{v_\theta}{r} \right) + U_\phi^* \frac{\partial}{\partial r} \left(\frac{v_\phi}{r} \right) \right] d\Omega,\end{aligned}$$

where we recognize the stress-free condition in the last two terms of the surface integral and we eliminate them. In the remaining terms, we set $\mathbf{v} = \mathbf{u}$, so that:

$$\int_{core} \mathbf{U}^* \cdot \mathbf{L} \, dV = -\int_{core} \nabla \times \mathbf{U}^* \cdot \nabla \times \mathbf{u} \, dV + 2 \oint_{CMB} (U_\theta^* u_\theta + U_\phi^* u_\phi) \, d\Omega,$$

The total viscous integral is then:

$$\overline{\mathcal{G}} + \mathcal{G}_0 + \widetilde{\mathcal{G}} = -\int_{core} \nabla \times \mathbf{U}^* \cdot \nabla \times \mathbf{v}\, \mathrm{d}V + 2\oint_{CMB} (U_\theta^* u_\theta + U_\phi^* u_\phi)\, \mathrm{d}\Omega - \int_{core} \nabla \cdot \left[\Psi^* \frac{w_\Psi}{2H} \hat{\mathbf{z}} \times \mathbf{L}\right] \mathrm{d}V. \tag{C2}$$

We finally have to consider the third integral on the right-hand side of this last expression:

$$-\int_{core} \nabla \cdot \left[\Psi^* \frac{w_\Psi}{2H} \hat{\mathbf{z}} \times \mathbf{L}\right] dV = -\oint_{CMB} \hat{\boldsymbol{r}} \cdot \left[\Psi^* \frac{w_\Psi}{2H} \hat{\mathbf{z}} \times \mathbf{L}\right] d\Omega = \oint_{CMB} \Psi^* \frac{w_\Psi}{2H} L_\phi \sin\theta\, d\Omega$$
$$= -\oint_{CMB} \nabla \times \left[\Psi^* \frac{w_\Psi}{2H} \sin\theta\, \hat{\boldsymbol{\phi}}\right] \cdot \boldsymbol{\omega}\, d\Omega + \oint_{CMB} \nabla \cdot \left[\Psi^* \frac{w_\Psi}{2H} \sin\theta\, \hat{\boldsymbol{\phi}} \times \boldsymbol{\omega}\right] d\Omega.$$

The second integrals requires applying Gauss' theorem on a surface in 3-D space. We make use of formulae from appendix 7 of Backus *et al.* (1996). Let us define:

$$\Psi^* \frac{w_\Psi}{2H} \sin\theta\, \hat{\boldsymbol{\phi}} \times \boldsymbol{\omega} \equiv \mathbf{q} = \underbrace{\hat{\boldsymbol{r}} q_r}_{\text{normal}} + \underbrace{\mathbf{q}_h}_{\text{tangential}}.$$

We therefore need the following:

$$\oint_{CMB} \nabla \cdot \mathbf{q}\, d\Omega = \oint_{CMB} \left[\frac{1}{r^2}\frac{\partial}{\partial r}(r^2 q_r) + \nabla_h \cdot \mathbf{q}_h\right] d\Omega,$$

where ∇_h is the tangential gradient on the spherical surface of the CMB. According to eq. (7.4.21) of Backus *et al.* (1996), the second term in the above integral is zero, when integrated on the CMB. We therefore obtain:

$$\oint_{CMB} \nabla \cdot \left[\Psi^* \frac{w_\Psi}{2H} \sin\theta\, \hat{\boldsymbol{\phi}} \times \boldsymbol{\omega}\right] d\Omega = -\oint_{CMB} \frac{1}{r^2}\frac{\partial}{\partial r}\left[\Psi^* \frac{w_\Psi}{2} |\tan\theta| \omega_\theta r^2\right] d\Omega$$
$$= -\oint_{CMB} \frac{1}{r^2}\frac{\partial}{\partial r}\left[\Psi^* \frac{w_\Psi}{2} |\tan\theta| r^2\right] \omega_\theta d\Omega - \oint_{CMB} \Psi^* \frac{w_\Psi}{2} |\tan\theta| \frac{\partial \omega_\theta}{\partial r} d\Omega.$$

Therefore, the last integral in eq. (C2) is:

$$-\int_{core} \nabla \cdot \left[\Psi^* \frac{w_\Psi}{2H} \hat{\mathbf{z}} \times \mathbf{L}\right] dV = -\oint_{CMB} \nabla \times \left[\Psi^* \frac{w_\Psi}{2H} \sin\theta\, \hat{\boldsymbol{\phi}}\right] \cdot \boldsymbol{\omega}\, d\Omega$$
$$-\oint_{CMB} \frac{1}{r^2}\frac{\partial}{\partial r}\left[\Psi^* \frac{w_\Psi}{2} |\tan\theta| r^2\right] \omega_\theta d\Omega$$
$$-\oint_{CMB} \Psi^* \frac{w_\Psi}{2} |\tan\theta| \frac{\partial \omega_\theta}{\partial r} d\Omega$$

and now we apply the stress-free boundary condition. In the above expression, only ω_r, ω_θ and $\partial\omega_\theta/\partial r$ appear, which can be manipulated by applying the non-penetration and stress-free conditions eqs (6) and (8), where relevant:

$$\omega_r = \frac{1}{r\sin\theta}\left[\frac{\partial}{\partial\theta}(v_\phi \sin\theta) - \frac{\partial v_\theta}{\partial\phi}\right] = \frac{1}{r\sin\theta}\left[\frac{\partial}{\partial\theta}(u_\phi \sin\theta) - \frac{\partial u_\theta}{\partial\phi}\right],$$
$$\omega_\theta = -\frac{1}{r}\frac{\partial}{\partial r}(r v_\phi) + \frac{1}{r\sin\theta}\frac{\partial v_r}{\partial\phi} = -\frac{2}{r}u_\phi,$$
$$\frac{\partial\omega_\theta}{\partial r} = -\frac{\partial}{\partial r}\left(\frac{1}{r}\right) v_\phi - \frac{1}{r}\frac{\partial v_\phi}{\partial r} - \frac{\partial^2 v_\phi}{\partial r^2} + \frac{1}{\sin\theta}\frac{\partial}{\partial r}\left[\frac{1}{r}\frac{\partial v_r}{\partial\phi}\right] = -\frac{\partial^2 u_\phi}{\partial r^2} + \frac{1}{\sin\theta}\frac{\partial}{\partial r}\left[\frac{1}{r}\frac{\partial u_r}{\partial\phi}\right].$$

Putting everything together, rearranging terms and setting $w_\Psi = 1$, we can now obtain formula (eq. 49):

$$\mathcal{G} = \mathcal{G}_{sf} = -\int_{core} \nabla \times \mathbf{U}^* \cdot \nabla \times \mathbf{u}\, dV + 2\oint_{CMB} (U_\theta^* u_\theta + U_\phi^* u_\phi)\, d\Omega$$
$$+\oint_{CMB} \left\{-\frac{\omega_r}{\sin\theta}\frac{\partial}{\partial\theta}\left[\Psi^* \frac{1}{2}\frac{\sin^2\theta}{|\cos\theta|}\right] + \Psi^* |\tan\theta| \left[\frac{1}{2}\frac{\partial^2 u_\phi}{\partial r^2} - \frac{1}{2\sin\theta}\frac{\partial}{\partial r}\left(\frac{1}{r}\frac{\partial u_r}{\partial\phi}\right) + u_\phi\right]\right\} d\Omega,$$

APPENDIX D: ANALYTICAL EXPRESSION OF THE DISSIPATION INTEGRAL

Here we derive an analytical expression for the integral (eq. 53). In particular we show that the diagonal terms identically vanish.

For the purposes of this proof we re-write the columnar modes velocity as:

$$\mathbf{u}_n^m = \frac{1}{H}\nabla \times \left[s^m H^3 P_n^{(3/2,m)}(2s^2 - 1)\mathrm{e}^{\mathrm{i}m\phi}\hat{\mathbf{z}}\right] - \frac{z}{H^3}\frac{\partial}{\partial\phi}\left[s^m H^3 P_n^{(3/2,m)}(2s^2 - 1)\mathrm{e}^{\mathrm{i}m\phi}\right]\hat{\mathbf{z}},$$

and, for brevity of notation, we also define an inner product of two vectors $\mathbf{x}$ and $\mathbf{y}$ as:

$$< \mathbf{x}, \mathbf{y} >= \int_{core} \mathbf{x} \cdot \mathbf{y}^* dV$$

We also introduce the dual-basis:

$$\mathbf{v}_n^m = \nabla \times \left[s^m P_n^{(-1/2,m)}(2s^2-1)\mathrm{e}^{\mathrm{i}m\phi}\hat{\mathbf{z}}\right],$$
$$\mathbf{w}_n^m = \nabla \times \nabla \times \left[s^m z\, P_n^{(-1/2,m)}(2s^2-1)\mathrm{e}^{\mathrm{i}m\phi}\hat{\mathbf{z}}\right].$$

The vector $\mathbf{w}_n^m$ has a z-component that is linear in z but other components that are independent of z. The vectors $\mathbf{v}_n^m$ lie entirely in the horizontal plane. When $n = 0$, the vectors $\mathbf{v}_0^m$ and $\mathbf{w}_0^m$ are parallel.

Note that:

$$\hat{\mathbf{z}}\cdot\mathbf{w}_n^m = C_{n-1}^m z\, P_{n-1}^{(3/2,m)}(2s^2-1)\mathrm{e}^{\mathrm{i}m\phi}, \qquad \hat{\mathbf{z}}\cdot\nabla\times\mathbf{v}_n^m = C_{n-1}^m P_{n-1}^{(3/2,m)}(2s^2-1)\mathrm{e}^{\mathrm{i}m\phi}$$

, where:

$$C_n^m = -2(3+2m+2n)(m+n+1),$$

as can be shown using the elementary properties of Jacobi polynomials (e.g. Arfken *et al.* 2011). The following orthogonality properties hold:

$$\begin{aligned}
&<\mathbf{u}_j^m, \mathbf{u}_k^{m'}> = A_1^{(j,m)}\delta_{j,k}\delta_{m,m'},\\
&<\mathbf{u}_j^m, \mathbf{v}_k^{m'}> = A_2^{(j,m)}\delta_{j,k-1}\delta_{m,m'},\\
&<\mathbf{u}_j^m, \mathbf{w}_k^{m'}> = A_3^{(j,m)}\delta_{j,k-1}\delta_{m,m'},\\
&<\mathbf{v}_j^m, \mathbf{w}_k^{m'}> = A_4^{(j,m)}\delta_{j,k}\delta_{m,m'},
\end{aligned} \tag{D1}$$

where $A_i^{(j,m)}$ are normalization constants. Additionally

$$<\mathbf{u}_j^m, \mathbf{w}_k^{m'}> = \frac{m}{3\mathrm{i}} <\mathbf{u}_j^m, \mathbf{v}_k^{m'}>, \tag{D2}$$

and

$$<\mathbf{u}_j^m, \mathbf{v}_{j+1}^m> = -4\pi \frac{(2j^2+5j+3)(2j+2m+3)}{(4j+2m+5)}\frac{\Gamma(j+3/2)\Gamma(j+m+2)}{\Gamma(j+2)\Gamma(j+m+5/2)}. \tag{D3}$$

Lemma We can write:

$$\nabla^2\mathbf{u}_j^m = \sum_{l=0}^{j} a_l^{(j,m)}\mathbf{v}_l^m + b_l^{(j,m)}\mathbf{w}_l^m. \tag{D4}$$

Note the upper limit for the sum comes about since the maximum degree (in s) of $\nabla^2\mathbf{u}_j^m$ is $2j$, and hence is described by $\mathbf{v}_l^m$ and $\mathbf{w}_l^m$ with $l \le j$. The coefficients are given by (when $l \ge 1$):

$$\begin{aligned}
b_l^{(j,m)} &= \frac{\mathrm{i}m}{4}(j-l+1)(4l+2m+1)(2j+2l+2m+3)\frac{\Gamma(l+1/2+m)\Gamma(j+m+1)}{\Gamma(l+1+m)\Gamma(j+m+5/2)},\\
a_l^{(j,m)} &= b_l^{(j,m)}\frac{\mathrm{i}}{m}(4j^2+4jm+10j+5m+6).
\end{aligned} \tag{D5}$$

Proof To prove the above-given lemma, it is sufficient to show agreement of both sides of eq. (D4) in both the vertical component and the vertical component of the curl, since both the left and right hand sides are divergence-free vectors and can be written in a toroidal-poloidal form. Thus, we show that:

$$\hat{\mathbf{z}}\cdot\nabla^2\mathbf{u}_j^m = \sum_{l=0}^{j} b_l^{(j,m)}\hat{\mathbf{z}}\cdot\mathbf{w}_l^m, \qquad \hat{\mathbf{z}}\cdot\nabla\times\nabla^2\mathbf{u}_j^m = \sum_{l=0}^{j} a_l^{(j,m)}\hat{\mathbf{z}}\cdot\nabla\times\mathbf{v}_l^m.$$

By the properties of the dual basis, these can be written as:

$$\hat{\mathbf{z}}\cdot\nabla^2\mathbf{u}_j^m = z\, s^m\mathrm{e}^{\mathrm{i}m\phi}\textstyle\sum_{l=0}^{j} C_{l-1}^m b_l^{(j,m)} P_{l-1}^{(3/2,m)}(2s^2-1)\mathrm{e}^{\mathrm{i}m\phi}, \tag{D6}$$

$$\hat{\mathbf{z}}\cdot\nabla\times\nabla^2\mathbf{u}_j^m = s^m\mathrm{e}^{\mathrm{i}m\phi}\textstyle\sum_{l=0}^{j} C_{l-1}^m a_l^{(j,m)} P_{l-1}^{(3/2,m)}(2s^2-1)\mathrm{e}^{\mathrm{i}m\phi}. \tag{D7}$$

We can show eqs (D6) and (D7) by explicitly calculating the expansions on both sides of each equation, using:

$$P_n^{(\alpha,\beta)}(x) = \frac{\Gamma(n+\alpha+1)}{\Gamma(n+1)\Gamma(\alpha+\beta+n+1)}\sum_{k=0}^{n}\frac{\Gamma(n+1)\Gamma(\alpha+\beta+n+k+1)}{\Gamma(k+1)\Gamma(n-k+1)\Gamma(\alpha+k+1)}\left(\frac{x-1}{2}\right)^k. \tag{D8}$$

For example, for the right-hand-side of eq. (D6) writing:

$$\sum_{l=0}^{j} C_{l-1}^m b_l^{(j,m)} P_{l-1}^{(3/2,m)}(2s^2-1),$$

as an expansion in powers of $y = (x-1)/2 = s^2 - 1$ (since in the above $x = 2s^2 - 1$), and performing the summation (over l), gives the following expression for the coefficient of y^r, where r is an integer:

$$S_{jmr} = \frac{-64\mathrm{i}m(j+m)4^r}{\sqrt{\pi}(8r^3+60r^2+142r+105)} \frac{\Gamma(j+7/2)\Gamma(j+m+7/2+r)}{\Gamma(j-r)\Gamma(2+2r)\Gamma(j+m+5/2)}. \tag{D9}$$

We note in passing that:

$$\sum_{r=0}^{j} y^r S_{jmr} = K_1 P_{j-1}^{(7/2,m)}(2s^2-1),$$

where K_1 is a proportionality constant. To find the left-hand-side of eq. (D6), we use the usual derivative-forms of the Jacobi polynomials:

$$\frac{d^k}{dx^k} P_n^{(\alpha,\beta)}(x) = \frac{\Gamma(\alpha+\beta+n+1+k)}{2^k\Gamma(\alpha+\beta+n+1)} P_{n-k}^{(\alpha+k,\beta+k)}(x),$$

leading to:

$$\hat{\mathbf{z}}\cdot\nabla^2\mathbf{u}_j^m = -\mathrm{i}m(2m+2n+5)\left[(x+1)(7/2+m+n)P_{n-2}^{(3/2+2,m+2)}(x) + 2(m+1)P_{n-1}^{(3/2+1,m+1)}(x)\right]\mathrm{e}^{\mathrm{i}m\phi},$$

where $x = 2s^2 - 1$. Using eq. (D8) again, and collecting together the coefficients of $s^2 - 1$, we obtain eq. (D9). Thus the two sides of eq. (D6) are equal.

A derivation of eq. (D7) follows along identical lines, although it is more involved as the expressions involve higher derivatives. In this case, the analogue of eq. (D9), the coefficient of y^r, is $S_{jmr}/(-\mathrm{i}m)$.

Theorem The elements of the integral $< \mathbf{u}_k^m, \nabla^2\mathbf{u}_j^m >$ are zero if $k \geq j$, and are positive-definite when $k < j$. In particular, for $k < j$:

$$< \mathbf{u}_k^m, \nabla^2\mathbf{u}_j^m > = \frac{4\pi}{3}(j-k)(2j+2k+2m+5)(12j^2+12jm+m^2+30j+15m+18)\frac{\Gamma(j+m+1)\Gamma(k+5/2)}{\Gamma(j+m+5/2)\Gamma(k+1)}. \tag{D10}$$

Usingeq. (D4) it follows that:

$$\begin{aligned} < \mathbf{u}_k^m, \nabla^2\mathbf{u}_j^{m'} > &= \sum_{l=0}^{j} (a_l^{(j,m)})^* < \mathbf{u}_k^m, \mathbf{v}_l^{m'} > + (b_l^{(j,m)})^* < \mathbf{u}_k^m, \mathbf{w}_l^{m'} > \\ &= \delta_{m,m'}\left((a_{k+1}^{(j,m)})^* < \mathbf{u}_k^m, \mathbf{v}_{k+1}^m > + (b_{k+1}^{(j,m)})^* < \mathbf{u}_k^m, \mathbf{w}_{k+1}^m > \right). \end{aligned}$$

which, by dint of eq. (D1) leads to:

$$< \mathbf{u}_k^m, \nabla^2\mathbf{u}_j^{m'} > = \begin{cases} \left[(a_{k+1}^{(j,m)})^* < \mathbf{u}_k^m, \mathbf{v}_{k+1}^m > + (b_{k+1}^{(j,m)})^* < \mathbf{u}_k^m, \mathbf{w}_{k+1}^m > \right]\delta_{m,m'} & \text{for } k < j \\ 0 & \text{for } k \geq j. \end{cases}$$

Using eqs (D2), (D3) and (D5) gives eq. (D10), which is positive definite when $k < j$.